The Astrophysical Journal, 910:121 (16pp), 2021 April 1 https://doi.org/10.3847/1538-4357/abe530

On the Color–Metallicity Relation of the Red Clump and the Reddening toward the Magellanic Clouds

David M. Nataf[1], Santi Cassisi[2,3], Luca Casagrande[4], Wenlong Yuan[1], and Adam G. Riess[1,5]
[1] Center for Astrophysical Sciences and Department of Physics and Astronomy, The Johns Hopkins University, Baltimore, MD 21218, USA; dnataf1@jhu.edu, david.nataf@gmail.com
[2] INAF-Osservatorio Astronomico d'Abruzzo, via M. Maggini, sn. I-64100 Teramo, Italy
[3] INFN-Sezione di Pisa, Largo Pontecorvo 3, I-56127 Pisa, Italy
[4] Research School of Astronomy and Astrophysics, Mount Stromlo Observatory, The Australian National University, ACT 2611, Australia
[5] Space Telescope Science Institute, 3700 San Martin Drive, Baltimore, MD 21218, USA
Received 2020 March 27; revised 2021 February 8; accepted 2021 February 9; published 2021 April 5

Abstract

The zero point of the reddening toward the Large Magellanic Cloud (LMC) has been the subject of some dispute. Its uncertainty propagates as a systematic error for methods that measure the extragalactic distance scale through knowledge of the absolute extinction of LMC stars. In an effort to resolve this issue, we used three different methods to calibrate the most widely used metric to predict LMC extinction, the intrinsic color of the red clump, $(V-I)_{RC,0}$, for the inner $\sim 3^\circ$ of that galaxy. The first approach was to empirically calibrate the color zero points of the BaSTI isochrones over a wide metallicity range of $\Delta[\mathrm{Fe/H}] \approx 1.10$ using measurements of red clump stars in 47 Tuc, the solar neighborhood, and NGC 6791. From these efforts, we also measure these properties of the solar neighborhood red clump, $(V-I, G_{BP}-K_s, G-K_s, G_{RP}-K_s, J-K_s, H-K_s, M_I, M_{Ks})_{RC,0} =$ (1.02, 2.75, 2.18, 1.52, 0.64, 0.15, −0.23, −1.63). The second and third methods were to compare the observed colors of the red clump to those of Cepheids and RR Lyrae in the LMC. With these three methods, we estimated the intrinsic color of the red clump of the LMC to be $(V-I)_{RC,0,\mathrm{LMC}} = \{\approx \mathbf{0.93},\ 0.91 \pm 0.02,\ 0.89 \pm 0.02\}$, respectively, and similarly, using the first and third methods, we estimated $(V-I)_{RC,0,\mathrm{SMC}} = \{\approx \mathbf{0.85},\ 0.84 \pm 0.02\}$, respectively, for the Small Magellanic Cloud. We estimate the luminosities to be $M_{I,RC,\mathrm{LMC}} = -0.26$ and $M_{I,RC,\mathrm{SMC}} = -0.37$. We show that this has important implications for recent calibrations of the tip of the red giant branch in the Magellanic Clouds used to measure H_0.

Unified Astronomy Thesaurus concepts: Distance indicators (394); Stellar distance (1595); Horizontal branch (2048); Large Magellanic Cloud (903); Small Magellanic Cloud (1468); RR Lyrae variable stars (1410); RRab variable stars (1413); Cepheid variable stars (218); Stellar evolutionary models (2046)

1. Introduction

The red clump, which is the horizontal branch of a metal-rich ($[\mathrm{Fe/H}] \gtrapprox -1.0$) stellar population, is a long-lived and thus well-populated evolutionary stage and predicted by stellar theory to have precise color–metallicity and luminosity–metallicity relations (Girardi & Salaris 2001; Salaris & Girardi 2002). The red clump has thus been a widely used "standard crayon" and standard candle to characterize stellar populations over a wide range of ages, for example, the mapping of the chemical gradients of the Milky Way disk (Nidever et al. 2014); the mapping of the reddening toward the Milky Way's nuclear disk (Nogueras-Lara et al. 2020); the reddening variations (Nataf et al. 2016), bar morphology (Stanek et al. 1997), peanut/X-shape profile (Nataf et al. 2010; McWilliam & Zoccali 2010), and the long bar component (Wegg et al. 2015) of the Milky Way Bulge; the reddening toward the Magellanic Clouds (Haschke et al. 2011; Górski et al. 2020); and the reddening of the tip of the red giant branch (TRGB) for distance scale work (Jang & Lee 2017a, 2017b; Yuan et al. 2019) and the reddening of and distance to the Sagittarius stream (Correnti et al. 2010; Carrell et al. 2012) and the Andromeda galaxy (Stanek & Garnavich 1998; Cohen et al. 2018).

That is an impressive breadth of discovery and diagnostic power, and one which we expect may grow in the coming decade as several new observatories come online. Each of the James Webb Space Telescope, The Wide-Field Infrared Survey Telescope, the Giant Magellan Telescope, the Thirty Meter Telescope, and the European Extremely Large Telescope (Gilmozzi & Spyromilio 2007) will be maximally sensitive for wavelengths with $\lambda \gtrapprox 1\ \mu$m, a regime where red clump stars are intrinsically bright due to their cool ($T_{\mathrm{eff}} \approx 4500$ K) effective temperatures. For example, $M_{\mathrm{RC,Ks}} \approx -1.62$ for the stellar population of the solar neighborhood (Chen et al. 2017; Hawkins et al. 2017; Chan & Bovy 2020).

We have thus been motivated to explore a discrepancy in the assumed intrinsic red clump optical color $(V-I)_{RC,0}$ in the recent literature. The assumption directly affects the reddening toward the Large Magellanic Cloud (LMC), for which the widely used reddening map of Haschke et al. (2011) had assumed $(V-I)_{RC,0,\mathrm{LMC}} = 0.92$. This assumption is corroborated by other methods. For example, the reddening map of Inno et al. (2016), which is derived from measurements of classical Cepheids, estimated a reddening toward the LMC that was 0.02 mag greater in the mean, an offset smaller than the reported errors. However, the recent investigation of Górski et al. (2020) derived a much bluer value of $(V-I)_{RC,0,\mathrm{LMC}} = 0.838 \pm 0.034$ for the LMC. Stellar population gradients might also be an issue. Indeed, the investigation of Skowron et al. (2021), which was submitted at around the same time as our own, derived $(V-I)_{RC,0,\mathrm{LMC}} = 0.8915 - d \times 0.0025$, where d is the projected separation (in degrees) of a field with respect to the center of the LMC. In this work, we focus on the properties of the red clump in the inner few degrees of the LMC and SMC.

That offset, perhaps as large as 0.08 mag in $(V-I)_{RC,0,\mathrm{LMC}}$, is substantially larger than the reported errors of most, and indeed perhaps all, recent investigations that assume an intrinsic color for the red clump. It may be due to factors such as undiagnosed population effects in the LMC stellar population, or the red clump color–metallicity relation having a very different slope than commonly assumed. Either finding would necessitate a revision of much of the literature on stellar astrophysics, interstellar reddening, and the distance scale. It also might have a simpler explanation if the sight lines of the young, blue supergiants used by Górski et al. (2020) to deredden red clump stars are dustier than those of the older, red giants that we consider in Section 5.

The purpose of this work is to investigate the issue of the red clump's color–metallicity relation, and to derive robust zero points for the red clump for use in the LMC and the Small Magellanic Cloud (SMC). We first review the theoretical and empirical calibration of the red clump in Section 2. We verify the consistency of these estimates for the LMC and SMC in Section 3. In Section 4, we evaluate the consistency of the predicted value of $(V-I)_{RC,0}$ for the LMC and SMC with calibrations from exquisitely measured Cepheids and RRab stars. We discuss our findings and present our conclusions in Sections 5 and 6.

2. Calibration of the Red Clump

In this section, we will employ a hybrid empirical and theoretical approach to predict the color and magnitude of the red clumps of the LMC and SMC. We will follow the approach of Girardi & Salaris (2001) and Salaris & Girardi (2002), in which the trends of the red clump color and magnitude with age and metallicity are derived from stellar models, but the zero points are shifted to agree with the best available empirical data.

The red clumps of the globular cluster 47 Tuc, of the solar neighborhood, and of the open cluster NGC 6791 will be used to calibrate the zero points. For each of those three stellar populations and both Magellanic Clouds, we will state both our assumed population parameters ([Fe/H], $[\alpha/\mathrm{Fe}]$, etc.), as well as other robust estimates from the literature, as the uncertainty in population parameters contributes to the uncertainty in the overall calibration.

For the chemical abundances ([Fe/H], $[\alpha/\mathrm{Fe}]$), we assume the parameters derived by the ASPCAP pipeline (García Pérez et al. 2016) from spectra taken for APOGEE (Majewski et al. 2017), a high-resolution ($R\sim 22,\ 500$), high signal-to-noise (S/N $\sim$100) Galactic archeology spectroscopic survey that is part of the Sloan Digital Sky Survey (Blanton et al. 2017). This survey is chosen as it has a large number of consistent measurements of the stellar populations studied in this work. The [Fe/H] abundances are consistent with prior literature values, with a mean and standard deviation in the offset with respect to 525 "standard stars" of $\Delta[\mathrm{Fe/H}]=0.04\pm0.10$ dex, and is largely a uniform shift, without a metallicity trend (Table 4 and Figure 3 of Jönsson et al. 2018, respectively). We also verify that this is the case for the particular populations studied in this work. We use these abundances not just for the LMC and SMC, but for all stellar populations discussed in this work, to ensure a homogeneous metallicity scale.

2.1. Population Parameters for the Large and Small Magellanic Clouds

We assume the star formation histories measured by Weisz et al. (2013), which can be read off their Figures 4 and 5 and were also kindly sent to us by email. These star formation histories were derived by comparing deep color–magnitude diagrams observed with HST, with synthetic color–magnitude diagrams created by MATCH (Dolphin 2002). The resulting mean ages for the LMC and SMC stellar populations are 6 and 5 Gyr respectively.

Seven of the eight LMC fields, and three of the four SMC fields, studied by Weisz et al. (2013) are toward sight lines closer to the centers of those galaxies than the majority of the tracers we use in this work. Based on their Figure 4, we may thus be underestimating the age by $\sim$1 Gyr. As we will show in Section 2.2, this would have a negligible effect on the derived red clump color and a 0.03 mag effect on the predicted red clump brightness.

Regardless of how they are weighted over the different star formation histories, these age estimates are not consistent with several prior literature results. A significant contributor to this difference is that the mean age of the stellar population need not be the same as the mean age of stars in the red clump region of the color–magnitude diagram, a correction that we explain and account for in Section 2.3. For example, Rubele et al. (2018) derived $\tau_{\mathrm{SMC}}\approx 3$ Gyr for stars in and near the red clump (Region D panel of their Figure 13), and Choi et al. (2018) derived $\tau_{\mathrm{LMC}}\approx 1.6$ Gyr by assuming $[\mathrm{Fe/H}]=-0.50$ and the age–metallicity relation of Carrera et al. (2008). Yanchulova Merica-Jones et al. (2017) did derive a $\sim$2 Gyr mean age for the red clump of the SMC using a more comprehensive color–magnitude diagram.

On the other hand, some prior literature estimates were more consistent with ours, or even derived an older age. Piatti & Geisler (2013) estimated the ages and metallicities of LMC red giants, from which they derive $\tau=5$ Gyr at [Fe/H] -0.70, their mean LMC metallicity for stellar populations at projected separations similar to those studied in this work. Nidever et al. (2020) fit a chemical evolution model to LMC abundance data, from which they derived a mean age of $\tau\approx 10$ Gyr for the LMC.

We use the abundances of faint red giants and bright red giants, as defined by Nidever et al. (2020) for the APOGEE LMC fields of LMC{4,5,6,8,9,13,14} and SMC fields of SMC {3,4,5}. We exclude stars with $\log g\geqslant 2$ as likely being foreground contaminants and stars with $[\mathrm{Fe/H}]\leqslant -1.1$ as likely not contributing to the red clump. This yields a sample of 882 red giants in the LMC and 310 red giants in the SMC. The resulting mean values of ($\langle[\mathrm{Fe/H}]\rangle$, $\langle[\alpha/\mathrm{Fe}]\rangle$) are ($-0.64$, $+0.03$) and (-0.88, -0.02) for the LMC and SMC, respectively, with a mean angular separation from the centers of their host galaxies of $2\overset{\circ}{.}8$ and $1\overset{\circ}{.}6$, respectively. A cut at $[\mathrm{Fe/H}]\leqslant -1.5$ would shift the effective mean metallicities by 0.04 and 0.08 dex for the LMC and SMC, respectively. The mean metallicity derived in the investigation of Weisz et al. (2013) is nearly identical, for example, ($\langle[\mathrm{Fe/H}]_{\mathrm{LMC}}\rangle=-0.63$.

These are consistent with other literature values. From the work of Van der Swaelmen et al. (2013), we find that the mean abundance of 148 LMC bar and disk stars satisfying $[\mathrm{M/H}]\geqslant -1.1$ is $\langle[\mathrm{M/H}]\rangle=-0.64$. Similarly, from the work of Parisi et al. (2016), we find an abundance of

$\langle[\mathrm{Fe/H}]\rangle = -0.81$ for the SMC, and Mucciarelli (2014) reported $\langle[\alpha/\mathrm{Fe}]\rangle \approx +0.10$.

The full list of adopted population parameters, for all stellar populations discussed in this work, can be found in Table 3.

2.2. Theoretical Calibration of the Red Clump

For theoretical predictions of the color of the red clump, we use the isochrones from the BaSTI database[6] for both the scaled-solar and α-enhanced ($[\alpha/\mathrm{Fe}] = +0.40$) cases (Pietrinferni et al. 2004, 2006; Cordier et al. 2007). We use the models with the suggested opacities (Ferguson et al. 2005) and with a red giant mass-loss parameter of $\eta = 0.20$ (Reimers 1975). This value has been validated by Miglio et al. (2012) in their study of NGC 6791 and 6819, two open clusters for which there are asteroseismic data. They reported that the data were consistent with a mass-loss parameter of $0.10 \lesssim \eta \lesssim 0.30$. We use isochrones with the metallicities $[\mathrm{M/H}] = \{-0.66, -0.35, -0.25, +0.06, +0.26, +0.40\}$ and ages $\tau/\mathrm{Gyr} = \{2.5, 5.0, 10.0, 12.0\}$; we also include isochrones with $([\mathrm{Fe/H}], [\alpha/\mathrm{Fe}]) = (-0.96, 0.00)$.

The predicted mean color and mean magnitude of the red clump are derived by computing the weighted mean of all equivalent evolutionary points that are no brighter than 0.07 mag brighter than the red clump and that correspond to evolutionary stages subsequent to the helium flash. Adjusting the 0.07 mag criterion by 0.01 or 0.02 mag has a negligible impact ($\approx$0.001 mag) on the derived predicted color and magnitude of the red clump. The full list of predicted magnitudes and colors can be found in Table 1 and is plotted in Figure 1.

We find that the dependence of magnitude and color on population parameters cannot be adequately fit for with a simple function over the full parameter space. For example, the dependence of $(V-I)_{RC,0}$ on age is itself a function of metallicity; see Figure 1. In order to estimate the prediction for the LMC directly from the isochrones, without first deriving empirically calibrated offsets, we compute a linear fit over a limited parameter range, with $[\mathrm{Fe/H}] \leqslant -0.25$, $2.5 \leqslant \tau/\mathrm{Gyr} \leqslant 10$:

$$(V-I)_{RC,0,\mathrm{LMC}} \approx 0.92 + 0.20([\mathrm{Fe/H}]_{\mathrm{LMC}} + 0.64) + 0.12([\alpha/\mathrm{Fe}]_{\mathrm{LMC}} - 0.03) + 0.01\log(\tau_{\mathrm{LMC}}/6\ \mathrm{Gyr}) \quad (1)$$

$$M_{I,RC,\mathrm{LMC}} \approx -0.42 + 0.19([\mathrm{Fe/H}]_{\mathrm{LMC}} + 0.64) + 0.06([\alpha/\mathrm{Fe}]_{\mathrm{LMC}} - 0.03) + 0.36\log(\tau_{\mathrm{LMC}}/6\ \mathrm{Gyr}), \quad (2)$$

where the x intercepts are chosen to correspond to the population parameters of the LMC. Similarly for the SMC, we compute a linear fit over a limited parameter range, with $[\mathrm{Fe/H}] \leqslant -0.60$, $\tau/\mathrm{Gyr} \leqslant 10$:

$$(V-I)_{RC,0,\mathrm{SMC}} \approx 0.87 + 0.18([\mathrm{Fe/H}]_{\mathrm{SMC}} + 0.88) + 0.09([\alpha/\mathrm{Fe}]_{\mathrm{SMC}} + 0.02) + 0.00\log(\tau_{\mathrm{SMC}}/5\ \mathrm{Gyr}) \quad (3)$$

$$M_{I,RC,\mathrm{SMC}} \approx -0.50 + 0.15([\mathrm{Fe/H}]_{\mathrm{SMC}} + 0.88) + 0.07([\alpha/\mathrm{Fe}]_{\mathrm{SMC}} + 0.02) + 0.39\log(\tau_{\mathrm{SMC}}/5\ \mathrm{Gyr}). \quad (4)$$

The scatter between the model-predicted values and the fit-predicted values is $\sim$0.01 mag.

[6] http://basti.oa-abruzzo.inaf.it/index.html

Table 1
The Mean Magnitude and Color of the Red Clump as Predicted by the BaSTI Isochrones for a Range of Population Abundances and Ages

[Fe/H]	[α/Fe]	τ/Gyr	$M_{I,RC}$	$(V-I)_{RC,0}$
−1.01	0.40	2.50	−0.61	0.89
−1.01	0.40	5.00	−0.51	0.89
−1.01	0.40	10.00	−0.37	0.88
−1.01	0.40	12.00	−0.31	0.86
−0.96	0.00	2.50	−0.65	0.87
−0.96	0.00	5.00	−0.53	0.87
−0.96	0.00	10.00	−0.36	0.85
−0.96	0.00	12.00	−0.29	0.83
−0.70	0.40	2.50	−0.55	0.94
−0.70	0.40	5.00	−0.46	0.95
−0.70	0.40	10.00	−0.33	0.94
−0.70	0.40	12.00	−0.29	0.94
−0.66	0.00	2.50	−0.59	0.91
−0.66	0.00	5.00	−0.48	0.92
−0.66	0.00	10.00	−0.34	0.91
−0.66	0.00	12.00	−0.29	0.89
−0.60	0.40	2.50	−0.52	0.96
−0.60	0.40	5.00	−0.43	0.97
−0.60	0.40	10.00	−0.32	0.97
−0.60	0.40	12.00	−0.28	0.96
−0.35	0.00	2.50	−0.50	0.96
−0.35	0.00	5.00	−0.40	0.97
−0.35	0.00	10.00	−0.29	0.97
−0.35	0.00	12.00	−0.25	0.97
−0.29	0.40	2.50	−0.45	1.03
−0.29	0.40	5.00	−0.37	1.06
−0.29	0.40	10.00	−0.27	1.07
−0.29	0.40	12.00	−0.24	1.06
−0.25	0.00	2.50	−0.46	0.98
−0.25	0.00	5.00	−0.38	0.99
−0.25	0.00	10.00	−0.27	1.00
−0.25	0.00	12.00	−0.23	0.99
−0.09	0.40	2.50	−0.42	1.09
−0.09	0.40	5.00	−0.34	1.12
−0.09	0.40	10.00	−0.25	1.13
−0.09	0.40	12.00	−0.22	1.13
0.05	0.40	2.50	−0.41	1.14
0.05	0.40	5.00	−0.34	1.18
0.05	0.40	10.00	−0.25	1.19
0.05	0.40	12.00	−0.22	1.20
0.06	0.00	2.50	−0.36	1.04
0.06	0.00	5.00	−0.28	1.07
0.06	0.00	10.00	−0.19	1.08
0.06	0.00	12.00	−0.16	1.08
0.25	0.00	2.50	−0.32	1.09
0.25	0.00	5.00	−0.24	1.12
0.25	0.00	10.00	−0.15	1.14
0.25	0.00	12.00	−0.12	1.14
0.40	0.00	2.50	−0.30	1.13
0.40	0.00	5.00	−0.22	1.16
0.40	0.00	10.00	−0.14	1.19
0.40	0.00	12.00	−0.11	1.19

The predicted theoretical dependence of $(V-I)_{RC,0}$ on age and metallicity is plotted in Figure 1, where we also show the empirical measurements for our three calibrating populations and the previously assumed parameters for the LMC and SMC.

We did verify how increasing the color range to red to include the first ascent red giant branch would shift the derived colors. That is in principle more appropriate for composite populations such as the LMC, the SMC, and the solar neighborhood, for which the red clump is inevitably mixed

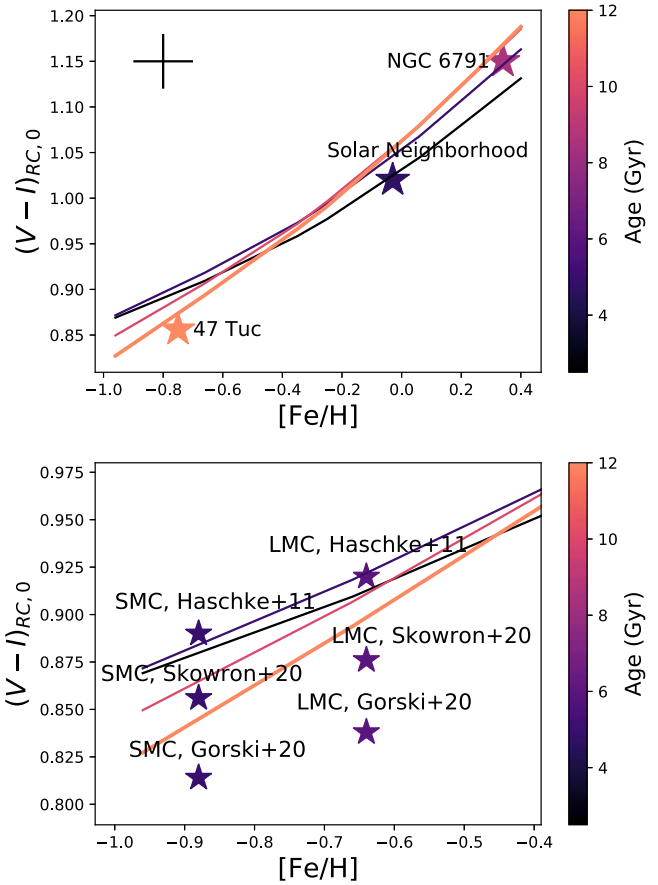

Figure 1. The BaSTI-predicted values of $(V-I)_{RC,0}$ as a function of [Fe/H] for $[\alpha/\mathrm{Fe}]=0$ and $\tau/\mathrm{Gyr}=(2.5, 5.0, 10.0, 12.0)$, shown as the curves that are color-coded by age. We show the $(V-I)_{RC,0}$ values for three calibrating stellar populations as asterisks color-coded for ages, with a characteristic error bar shown in the top left of the plot. The adopted values of [Fe/H], age, etc. are justified in Section 2.4. The $(V-I)_{RC,0}$ of 47 Tuc is shifted by 0.025 mag due to its elevated α-element and initial helium abundance. The measured values of $(V-I)_{RC,0}$ are on average 0.03 ± 0.01 mag lower (bluer) than the BaSTI-predicted values. A zoom-in of the lower-metallicity relationship is shown in the bottom panel, where we also show, as asterisks color-coded for age, the $(V-I)_{RC,0}=0.89$, 0.92 values assumed by Haschke et al. (2011), the $(V-I)_{RC,0}\approx0.885$, 0.862 values assumed by Skowron et al. (2021) at the mean position of the red giant stars with spectroscopic metallicities used as calibrators here, and the $(V-I)_{RC,0}=0.814\pm0.034$, 0.838 ± 0.034 values assumed by Górski et al. (2020), with [Fe/H] and age assumptions justified in Section 2.1.

with the first ascent red giant branch. We found that the effect is small—the predicted $(V-I)_{RC,0}$ is increased by 0.005 mag. That is because of the relative number counts of the two phases. Nataf et al. (2014) computed, using the same isochrones as used here, that the equivalent width of the red clump above the underlying red giant luminosity function is approximately 2.0 mag.

We also list the predictions of the updated BaSTI database[2] (Hidalgo et al. 2018) for four metallicities. We downloaded isochrones with overshooting, diffusion, and mass-loss parameter $\eta=0.30$. This new version of the BaSTI model library represents a significant improvement with respect to the previous release. We refer to Hidalgo et al. (2018) for a detailed discussion on the various updates in both the input physics and numerical assumptions adopted for computing the new BaSTI stellar models. However, for the sake of completeness, here we mention that version 2 of BaSTI models is based on an updated solar heavy-element distribution (Caffau et al. 2011), updated nuclear reaction rates for both the H- and He-burning phases (see Pietrinferni et al. 2010 and references therein), revised outer boundary conditions, and updated conductive opacity evaluations (Cassisi et al. 2007), as well as an average mass-loss efficiency during the RGB stage constrained on the basis of asteroseismic benchmarks (Miglio et al. 2012). In particular, we note that the use of updated conductive opacity and a different mass-loss efficiency directly impacts on the red clump average color and magnitude, as will be shown in the following sections. Ideally, these isochrones would be used for all of the calculations, but their grid for the α-enhanced heavy-element distribution is not yet available. We also compute, for purposes of completeness, the predictions from the MIST[7] version 1.2 isochrones without rotation (Choi et al. 2016; Dotter 2016), and the predictions from the PARSEC[8] v1.2S isochrones with the YBC option for bolometric corrections and mass-loss parameter $\eta=0.2$ (Bressan et al. 2012; Chen et al. 2014; Tang et al. 2014; Chen et al. 2015).

The different predictions are listed in Table 2. Relative to the $[\mathrm{Fe/H}]\leqslant0$ predictions from the BaSTI v1 isochrones, the MIST v1.2 and PARSEC v1.2S predictions for the red clump from are slightly fainter and bluer ($\approx$0.02 mag), whereas the BaSTI v2 predictions are approximately 0.04 mag bluer and 0.12 mag fainter. The results are summarized in Table 2. From the four sets of models, and for parameter values approximately appropriate for the SMC and LMC, the predictions are of a $(V-I)_{RC,0}$ color that is approximately 0.02 ± 0.02 mag bluer, and of an $M_{I,RC}$ that is 0.04 ± 0.06 mag fainter, than that of the BaSTI v1 isochrones.

2.3. Composite Population Effects for the Magellanic Cloud Red Clumps

The mean color and brightness of the red clump of a stellar population need not necessarily correspond to the color and brightness of a red clump at the mean age and metallicity of a stellar population, as is assumed by Equations (1), (2), and (3) and (4). Among the contributing factors, stellar subpopulations with $0.50\lessapprox\tau/\mathrm{Gyr}\lessapprox2.0$ produce proportionately more red clump stars (see Figure 1 of Girardi & Salaris 2001 and the associated discussion for more details). Thus, on average, the red clump should be younger and more metal rich than the total stellar population.

To evaluate the amplitude of this correction for the LMC, we construct synthetic luminosity functions weighted by the star formation history of Weisz et al. (2013) and using the BaSTI v2 isochrones, due in part to their excellent online interpolation tools. This correction increases $(V-I)_{RC,0}$ by $\approx$0.03 mag, and increases $M_{I,RC}$ by ≈0.03 mag—in other words, the peak of the luminosity function becomes slightly redder and dimmer. The mean age of the stars in and near the red clump is between 3 and 4 Gyr, consistent with the arguments in Girardi (2016) and in Rubele et al. (2018). Estimates for the composite population effects of the SMC are excluded from this work due to their greater uncertainty, but we expect them to be comparable to or slightly greater than those for the LMC. We note that the estimates mean that ages for stars in the red clump region are slightly greater than those ($\tau\approx2$ Gyr) assumed by Yanchulova Merica-Jones et al. (2017) and Choi et al. (2018). We consider

[7] http://waps.cfa.harvard.edu/MIST/
[8] http://stev.oapd.inaf.it/cgi-bin/cmd

Table 2
The Predictions for the Absolute Magnitude and Color of the Red Clump as a Function of Age and Metallicity from Four Different Isochrone Libraries: BaSTI v1 (Pietrinferni et al. 2004; Cordier et al. 2007), BaSTI v2 (Hidalgo et al. 2018), MIST v1.2 (Choi et al. 2016; Dotter 2016), and PARSEC v1.2S (Bressan et al. 2012; Chen et al. 2014; Tang et al. 2014; Chen et al. 2015)

[Fe/H]	τ/Gyr	$M_{I,RC}$	$(V-I)_{RC,0}$	$M_{I,RC}$	$(V-I)_{RC,0}$	$M_{I,RC}$	$(V-I)_{RC,0}$	$M_{I,RC}$	$(V-I)_{RC,0}$
Parameters		BaSTI v1		BaSTI v2		MIST v1.2		PARSEC v1.2S	
−0.96	5.00	−0.53	0.87	−0.44	0.84	−0.51	0.85	−0.54	0.84
−0.96	10.00	−0.36	0.85	−0.18	0.79	−0.34	0.83	−0.38	0.83
−0.66	5.00	−0.48	0.92	−0.38	0.89	−0.46	0.90	−0.45	0.90
−0.66	10.00	−0.34	0.91	−0.18	0.86	−0.32	0.89	−0.27	0.88
−0.35	5.00	−0.40	0.97	−0.31	0.95	−0.39	0.96	−0.40	0.98
−0.35	10.00	−0.29	0.97	−0.15	0.94	−0.27	0.96	−0.28	0.98
0.06	5.00	−0.28	1.07	−0.17	1.05	−0.27	1.07	−0.26	1.11
0.06	10.00	−0.19	1.08	−0.04	1.06	−0.15	1.08	−0.16	1.12
0.25	5.00	−0.24	1.12	−0.11	1.11	−0.18	1.14	−0.21	1.17
0.25	10.00	−0.15	1.14	0.01	1.12	−0.07	1.16	−0.12	1.20

Note. A description of our application of these models can be found in Section 2.2.

this (arguably) small offset to be unsurprising, given the numerous remaining uncertainties. Were we to assume these ages, our derived color and magnitude for the LMC red clump would be slightly redder and brighter still.

2.4. Empirical Measurements of the Color of the Red Clump

In the prior section, we predicted the slope and zero point of the color–metallicity relation of the red clump. In this subsection, we use the measured color–magnitude diagrams of three stellar populations in the Milky Way to verify their accuracy. These are the globular cluster 47 Tuc (NGC 104), the solar neighborhood stellar population, and the open cluster NGC 6791. These populations are selected as they host numerous red clump stars, and they are well characterized in distance, reddening, and population parameters such as metallicity. They also provide a broad span in [Fe/H] which brackets the Magellanic Clouds. The color–magnitude diagrams of 47 Tuc and NGC 6791 are shown in Figure 2.

The population parameters that we adopt are derived from a range of methods and data sets. There is unfortunately no uniformly derived set of population parameters available across these different populations. Thus, we adopt the most tightly calibrated parameters available for the distances, reddening, metallicity, and age determinations (Table 2).

2.4.1. 47 Tuc

For 47 Tuc, we use the color–magnitude diagram of Bergbusch & Stetson (2009), and we restrict the sample to those stars with angular separation from the cluster center of $(\alpha,\ \delta) = (6.023625,\ -72.081276)$[9], in arcseconds, of $400 \leqslant \delta\psi \leqslant 900$, in order to reduce the effect of blending. We select the 241 red clump stars satisfying $0.84 \leqslant (V-I) \leqslant 0.99$ and $12.85 \leqslant I \leqslant 13.25$, for a mean apparent photometry of $(V-I)_{RC} = 0.927 \pm 0.002$ and $I_{RC} = 13.139 \pm 0.004$. The value of this measured centroid is negligibly sensitive to the dimensions of the box, as shifting the box 0.02 mag in color or 0.03 mag in magnitude has a 0.001 mag effect on each of $(V-I)_{RC}$ and I_{RC}. We have verified that we would have obtained a nearly identical result, $(V-I)_{RC} = 0.913 \pm 0.001$ and $I_{RC} = 13.086 \pm 0.003$, if we had instead used the color–magnitude diagram of Sarajedini et al. (2007), which is obtained from highly accurate and highly precise Hubble Space Telescope observations in $F606W$ and $F814$ transformed into V and I using theoretical transformations. The slightly bluer and brighter horizontal branch is likely due to the gradient in helium enrichment in the cluster (Nataf et al. 2011; Milone et al. 2012).

For the apparent distance, reddening to, and age of 47 Tuc, we adopt the values of $(m-M)_V = 13.370 \pm 0.015$, $E(V-I) = 0.045 \pm 0.01$, and $\tau = 12.0$ Gyr from Thompson

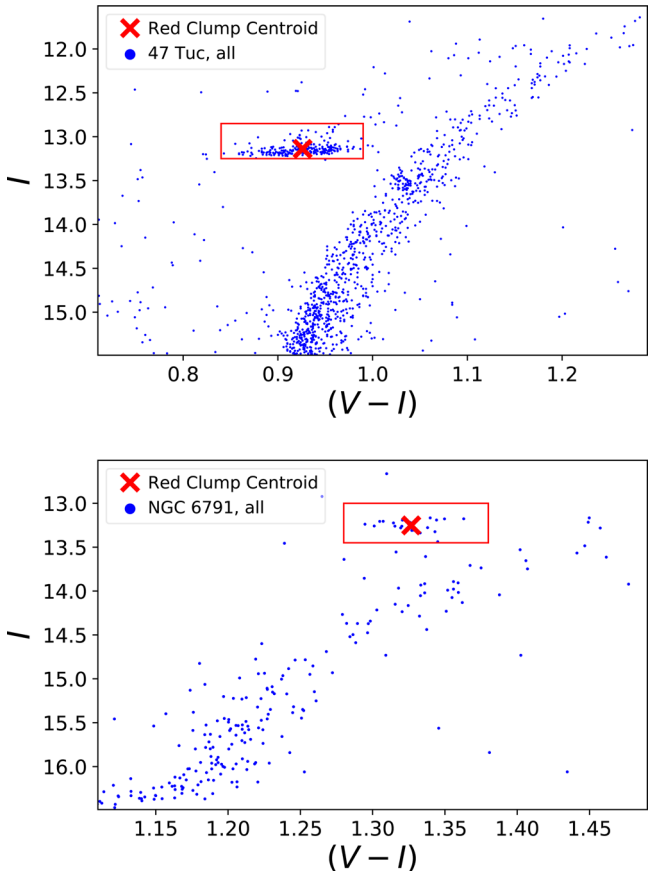

Figure 2. The color–magnitude diagrams of 47 Tuc (top) and NGC 6791 (bottom). The stars selected as being part of the red clump are plotted in the red rectangles.

[9] Taken from https://people.smp.uq.edu.au/HolgerBaumgardt/globular/orbits.html. For details, see Baumgardt et al. (2019).

et al. (2020). These measurements are predominantly derived from spectroscopic and photometric measurements of two members of an eclipsing binary system. The value and error of the distance modulus are computed from the values of the four eclipsing binary members. That is somewhat unphysical, as the errors on those four individual distances are almost certainly correlated (or anticorrelated), but unfortunately, both the sign and amplitude of that correlation are unknown.

We estimate the population abundances from APOGEE spectra of 60 cluster stars, where we use the same cluster selection criteria as Nataf et al. (2019); we require $\log g \leqslant 3.0$; and we restrict the analysis to stars satisfying $[\mathrm{N/Fe}] \leqslant +0.35$, a parameter space for which the consistency of the ASPCAP pipeline with other literature estimates has been demonstrated (Jönsson et al. 2018). We obtain the median abundances of $[\mathrm{Fe/H}] = -0.75$ and $[\alpha/\mathrm{Fe}] = +0.26$.

Our assumed population parameters for 47 Tuc are consistent with other literature values. From Thygesen et al. (2014), Johnson et al. (2015), and Marino et al. (2016), we respectively find ([Fe/H], [Mg/Fe], [Ca/Fe]) = (−0.78, +0.44, +0.24), ([Fe/H], [Mg/Fe]) = (−0.73, +0.33), and $[\mathrm{Fe/H}] = -0.68$. The distance ($\mu = 13.29$; M. Rozyczka and A. Dotter, 2020, private communication) is a little higher than the value of $\mu = 13.23 \pm 0.02$ derived by Baumgardt et al. (2019) from Gaia DR2 data. Salaris et al. (2016) estimated $\mu \approx 13.33$ by matching the observed red clump stellar distribution with models constructed from the same stellar evolution code used in this work, but with a different prescription concerning the mass-loss efficiency during the red giant branch stage. Finally, Hansen et al. (2013) estimated an age of $\tau/\mathrm{Gyr} = 9.9 \pm 0.7$ from its white dwarf cooling sequence. Grundahl et al. (2002) used Stromgren photometry of the cluster to estimate $(m-M)_V = 13.33$, $E(B-V) = 0.04$, and an age of $\tau/\mathrm{Gyr} = 12$.

The stellar population of 47 Tuc is also characterized by a small spread in initial helium abundance, Y (di Criscienzo et al. 2010; Nataf et al. 2011; Milone et al. 2017, 2018). Indeed, Gratton et al. (2013) studied the spectra of 110 red clump stars in 47 Tuc and found the [Na/O] abundances—and thus by proxy, the initial helium abundances—were tightly anticorrelated with the $(B-V)_0$ colors. Salaris et al. (2016) showed that the standard deviation in color and magnitude of the red clump of 47 Tuc is matched well by varying the initial helium abundance of the cluster's stars to be uniformly distributed in the interval $Y \in [0.256, 0.286]$. Using the BaSTI database, we find that this will shift the predicted red clump to being bluer and brighter, by $(\Delta(V-I)_{RC,0},\ \Delta M_{I,RC}) = (-0.009,\ -0.042)$. We find the predicted properties of the red clump in 47 Tuc are thus $((V-I)_{RC,0},\ M_{I,RC}) = (0.899,\ -0.336)$. In contrast, the observed values are $((V-I)_{RC,0},\ M_{I,RC}) = (0.882,\ -0.186)$.

2.4.2. Solar Neighborhood

For the solar neighborhood, Chan & Bovy (2020) have measured mean values of $M_{\mathrm{RC,J}} = -1.019$ and $M_{\mathrm{RC,Ks}} = -1.622$. However, the selection function that they used assumes the APOGEE red clump catalog (Bovy et al. 2014), which incorporates spectroscopic priors. That may differ from the photometric definition of the red clump used for populations such as the LMC and SMC, which is an excess in the luminosity function of post-main-sequence stars at or very close to the location of the horizontal branch.

We produced a photometric selection of red clump stars in the solar neighborhood through the following steps. We used the Gaia (Collaboration et al. 2016) Data Release 2 (Lindegren et al. 2018) solar neighborhood measurements from the Gaia archive[10], where we used their cross-match to the 2MASS catalog (Skrutskie et al. 2006). We required *visibility_periods_used* > 5, *astrometric_excess_noise* < 1, and applied a zero-point offset to the parallaxes of $\delta_\pi = -0.054$ mas (Schönrich et al. 2019). We select nearby stars with precise parallax measurements, such that $\pi \geqslant 3$ and $\pi/\sigma_\pi \geqslant 100$.

We selected a low-reddening sample by requiring that the estimated reddening to the stars satisfies $E(g-r) \leqslant 0.04$ (Green et al. 2019), for a mean reddening of $\langle E(g-r)\rangle = 0.005$, or equivalently, $\langle E(J-K_s)\rangle = 0.003$ ($R_V = 3.1$; Fitzpatrick 1999). We use the fitting routine of Nataf et al. (2016) to measure the properties of the red clump sample as an excess in the luminosity function over that of red giant stars, a method first developed by Stanek et al. (1997) and Paczyński & Stanek (1998). This selects approximately 1500 red clump stars. We note that the stars used in our analysis are not themselves inputs into the 3D reddening maps of Green et al. (2019), as those maps are constructed from stars fainter than the saturation limits of Pan-STARRS 1 (Flewelling et al. 2020).

To link measurements in (J, K_s) to expected colors in (V,I), we use the color–color relations from Table 1 of Nataf et al. (2016) and linearly interpolate over a small interval, which are derived from the library of synthetic stellar colors of Casagrande & VandenBerg (2014).

Our best-fit values for the solar neighborhood red clump are thus $M_{\mathrm{RC,Ks}} = -1.63$, $\sigma_{M_{Ks}} = 0.14$, $(J-K_s) = 0.64$, $M_{\mathrm{RC,I}} = -0.23$, and $(V-I) = 1.02$, where the statistical errors are each less than 0.01 mag. The $((V-I)_{RC,0},\ M_{I,RC})$ compare well to the prior measurement of $M_{\mathrm{RC,I}} - 0.28$, and $(V-I) = 1.01$ from Paczyński & Stanek (1998), which was derived from Hipparcos data (Perryman et al. 1997). The zero-point shift in the parallaxes of $\delta_\pi = -0.054$ mas (Schönrich et al. 2019) shifts $M_{\mathrm{RC,Ks}}$ by 0.03 mag. If we instead adopt the distances of Bailer-Jones et al. (2018), who assume priors for Galactic geometry discussed in that work, a zero-point offset to the Gaia parallaxes of $\delta_\pi = -0.029$ (Lindegren et al. 2018), we obtain the same color, but a slightly brighter red clump, with $M_{\mathrm{RC,Ks}} = -1.64$. We thus suggest a 0.01 mag error on M_{Ks}, due to this ambiguity as to which small correction we should apply to the DR2 parallaxes.

We also derive the following colors for the solar neighborhood red clump by direct fitting to the Gaia and 2MASS data: $(G_{BP}-K_s) = 2.75$, $(G-K_s) = 2.18$, $(G_{RP}-K_s) = 1.52$, and $(H-K_s) = 0.15$.

The color–magnitude diagram of solar neighborhood stars selected to have low reddening, and the combined red giant and red clump luminosity function, is shown in Figure 3.

To compute the parameters for the solar neighborhood stellar populations, we start with the posterior age distributions for ∼20,000 APOGEE targets with Galactic positions satisfying $7 \leqslant R_{GC}/\mathrm{kpc} \leqslant 9$, and $|z| \leqslant 0.50$ kpc that were computed by Feuillet et al. (2019). We then used the Galactocentric positions derived by Queiroz et al. (2020) to reweigh this sample to have the same mean separation from the Galactic plane (∼52 pc) and the same standard deviation thereof (123 pc) of our photometric sample of red clump stars. ($\langle[\mathrm{Fe/H}]\rangle$, $\langle[\alpha/\mathrm{Fe}]\rangle$, $\langle\tau/\mathrm{Gyr}\rangle$) = (−0.03, +0.03, 4.7). The composite population corrections (as in

[10] https://gea.esac.esa.int/archive/

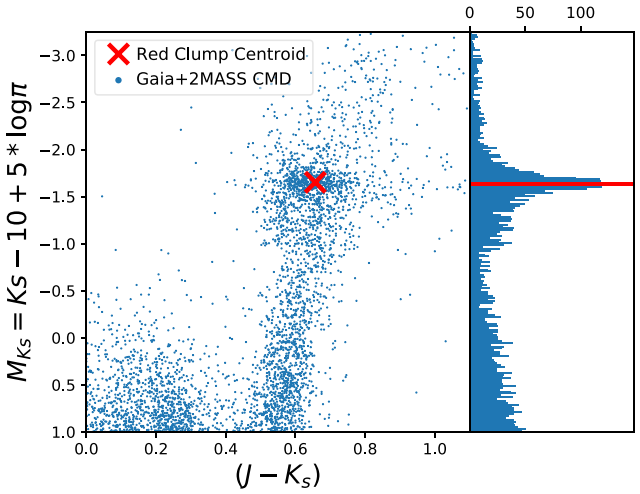

Figure 3. Left: the $(J - K_s,\ M_{Ks})$ color–magnitude diagram of solar neighborhood stars within ∼300 pc, with $\delta \geqslant -30°$. We plot every fifth data point for purposes of clarity. Right: the M_{Ks} luminosity function of the red giant branch stars; the red clump is measured to have a peak magnitude of $M_{Ks} = -1.63$.

Section 2.3) decreases $(V-I)_{RC,0}$, and decreases $M_{I,RC}$ by ≈0.03 mag—in other words, the peak of the luminosity function becomes slightly bluer and brighter.

These are remarkably similar to the values of $(\langle[Fe/H]\rangle, \langle[\alpha/Fe]\rangle, \langle\tau/Gyr\rangle) = (-0.04, +0.03, 5.1)$ that we derive by applying the same method to GALAH survey data (De Silva et al. 2015; Buder et al. 2019).

The predicted solar neighborhood red clump color and magnitude, assuming the parameters from Feuillet et al. (2019), fitting over the full span of Table 1 and applying the corrections for composite population effects, are $((V-I)_{RC,0},\ M_{I,RC}) = (1.03, -0.36)$. In contrast, the observed values are $((V-I)_{RC,0},\ M_{I,RC}) = (1.02, -0.25)$.

2.4.3. NGC 6791

For NGC 6791, we use the color–magnitude diagram of Stetson et al. (2003), which was updated for the work of Brogaard et al. (2012) and now includes corrections for differential reddening. We limit the selection to stars with Gaia-derived proper motions that are within 1.25 mas of the cluster central value of $\mu_\alpha \cos\delta,\ \mu_\delta = (-0.42, -2.28)$ reported by Donor et al. (2018). We select 24 red clump stars that have $1.24 \leqslant (V-I) \leqslant 1.38$ and $13.45 \leqslant I \leqslant 13.00$, for a mean apparent photometry of $((V-I)_{RC}, I_{RC})_{\rm NGC\ 6791} = (1.327 \pm 0.003, 13.252 \pm 0.013)$. The value of this measured centroid is negligibly sensitive to the dimensions of the box, as shifting the box to remove the bluest point, which does appear as the most uncertain point, reduces $(V-I)_{RC}$ by 0.002 mag and increases I_{RC} by 0.003 mag. The color–magnitude diagram of NGC 6791 is shown in the bottom panel of Figure 2.

The analysis of Brogaard et al. (2012), which incorporates information from the masses and radii of eclipsing binaries as well as the morphology of the three-bandpass color–magnitude diagram, yields the cluster parameters of $(m-M)_V = 13.51 \pm 0.06$, $E(V-I) = 0.17 \pm 0.02$, and $\tau = 8.3$ Gyr. The value and error of the distance modulus are computed from the values of the four eclipsing binaries listed in Table 1 of Brogaard et al. (2012). That is somewhat unphysical, as the errors on those four individual distances are almost certainly correlated (or anticorrelated), but unfortunately, both the sign and amplitude of that correlation are not available. From APOGEE spectra, the median abundances of 55 cluster stars with surface gravity $\log g \leqslant 3.0$ are $[Fe/H] = +0.34$, $[\alpha/Fe] = +0.04$.

These adopted population parameters are consistent with other literature values. Boesgaard et al. (2015) measured $(\langle[Fe/H]\rangle, \langle 1/5[O + Mg + Si + Ti + Ca/Fe]\rangle) = (+0.30, -0.02)$, and Villanova et al. (2018) measured $(\langle[Fe/H]\rangle, \langle 1/4[Mg + Si + Ti + Ca/Fe]\rangle) = (+0.31, +0.06)$. García-Berro et al. (2010) estimated an age of 8 Gyr from analysis of the cluster's white dwarf cooling sequence, and McKeever et al. (2019) estimated an age of $\tau/Gyr = 8.2$ from an asteroseismic analysis of the cluster's giants. One discrepant result is that of An et al. (2015), who applied the method of main-sequence fitting to BVI_cJHK_s photometric data of the cluster, and derived best-fit values of $[M/H] = +0.42$, $(m-M)_V = 13.38$, $E(V-I) = 0.137$, and $\tau/Gyr = 9.5$. Anthony-Twarog et al. (2007) used Stromgren photometry of the cluster to $[Fe/H] = +0.45$ $(m-M)_V = 13.60$, $E(B-V) = 0.155$, and an age of $\tau/Gyr = 7$.

Using predicted parameters from Table 3 satisfying $5 \leqslant \tau/Gyr \leqslant 10$ Gyr, $[Fe/H] \geqslant 0$, we find that the predicted NGC 6791 red clump has $((V-I)_{RC,0},\ M_{I,RC} = (1.17, -0.17))$. In contrast, the dereddened observed values are $((V-I)_{RC,0},\ M_{I,RC} = (1.15, -0.09)$.

2.5. A Combined Theoretical and Empirical Prediction for the Red Clumps of the Magellanic Clouds

The offsets between theory and data for the three stellar populations used in this work are highly consistent, which supports the use of empirical recalibration of the models. For 47 Tuc, the solar neighborhood, and NGC 6791, we measure red clumps that are respectively 0.02, 0.03, and 0.02 mag bluer in $(V-I)$, and 0.16, 0.09, and 0.09 mag fainter in M_I, relative to the model predictions, as listed in Table 1 and Equations (1), (2), (3), and (4). The offset between the data and the old BaSTI models is nearly equal to the offset between the old BaSTI models and the updated BaSTI models, where the latter are typically ∼0.03 mag bluer and ∼0.13 mag fainter.

Assuming these mean offsets of 0.02 mag and 0.13 mag, we derive predicted colors and magnitudes for the Magellanic Clouds of $((V-I)_{RC,0,LMC},\ M_{RC,I,LMC}) = (0.93, -0.26)$ and $((V-I)_{RC,0,SMC},\ M_{RC,I,SMC}) = (0.85, -0.25)$.

3. Verifying the Consistency of Our Absolute Magnitude and Intrinsic Color Calibrations

The independent calibrations of the absolute magnitude and intrinsic color of the red clump enable us to verify that our estimates are consistent with one another. By definition,

$$\mu = I_{RC} - M_{I,RC} - A_I, \tag{5}$$

where I_{RC} is the apparent magnitude of the red clump, and A_I is the extinction in the I band along a sight line. If we assume a standard extinction curve, then $A_I = 1.31E(V-I)$ ($R_V = 3.1$, Fitzpatrick 1999), and therefore

$$\mu = I_{RC} - M_{I,RC} - 1.31((V-I)_{RC} - (V-I)_{RC,0}). \tag{6}$$

We downloaded the OGLE-III photometry for the LMC field 100.1 (Udalski et al. 2008a). This sight line was selected to be toward the center of the LMC, enabling us to compare our

Table 3
In the Four Rightmost Columns, We Show Both the Best-fit Measured Intrinsic Parameters of the Red Clump and the BaSTI-predicted Parameters of the Red Clump

Population	[Fe/H]	[α/Fe]	τ/Gyr	$(m-M)_V$	$E(V-I)$	$(V-I)_{RC,0}$	$M_{I,RC}$	$(V-I)_{RC,\mathrm{BaSTI,v1}}$	$M_{I,RC,\mathrm{BaSTI,v1}}$
	Assumed Parameters					Derived Red Clump Centroid		Predicted Red Clump Centroid	
47 Tuc (NGC 104)	−0.75	+0.26	12	13.37	0.045	0.88	−0.18	0.90	−0.34
Large Magellanic Cloud	−0.64	+0.03	6	⋯	⋯	⋯	⋯	0.95	−0.39
Small Magellanic Cloud	−0.88	−0.02	5	⋯	⋯	⋯	⋯	0.87	−0.50
Solar Neighborhood	−0.03	+0.03	4.7	⋯	⋯	1.02	−0.23	1.03	−0.36
NGC 6791	+0.34	+0.04	8.3	13.51	0.174	1.15	−0.08	1.17	−0.17

Note. The measured parameters assume the distance and reddening values shown in the fifth and sixth columns, and the predicted parameters assume the chemistry and age values shown in the second, third, and fourth columns. For our three comparisons, the BaSTI-predicted values are on average 0.02 ± 0.01 mag redder in $(V-I)$ and 0.13 ± 0.03 mag brighter in M_I. All [Fe/H] and [α/Fe] values are homogeneously derived by ASPCAP (García Pérez et al. 2016) from APOGEE spectra (Majewski et al. 2017). The distance for the solar neighborhood sample are taken from Gaia (Collaboration et al. 2016) Data Release 2 (Lindegren et al. 2018) with a parallax zero-point offset of $\delta_\pi = -0.054$ mas derived by Schönrich et al. (2019) and with the reddening values taken from Green et al. (2019). The star formation histories of the SMC and LMC were derived by Weisz et al. (2013) from deep HST imaging, and their distances were derived by the detached eclipsing binary studies of Graczyk et al. (2014) and Pietrzyński et al. (2019). The ages, distances, and reddening to 47 Tuc and NGC 6791 were respectively derived by Thompson et al. (2020) and Miglio et al. (2012), for which the detached eclipsing binaries were responsible for the distance estimates.

result to the measured distance for that galaxy, without needing to correct for a geometric tilt.

We derive $\mu_{\mathrm{LMC}} = 18.45 \pm 0.02(\mathrm{stat}) \pm 0.04(\mathrm{sys})$, which is consistent with the value of $\mu_{\mathrm{LMC}} = 18.48$ measured from the analysis of 20 eclipsing binary systems (Pietrzyński et al. 2019). Among the potential systematic errors, a hypothetical uncertainty of 0.3 in R_V, of 0.01 in $(V-I)_{RC,0}$, and of 0.04 in $M_{I,RC}$, respectively, propagate as uncertainties of 0.01, 0.01, and 0.04 in the derived value of μ_{LMC}, for a combined systematic uncertainty of 0.04 mag. We show the color-magnitude diagram and luminosity function in Figure 4.

This method, when applied to the SMC photometry (Udalski et al. 2008b), did not yield as unambiguous a test as it did for the LMC. The red clump of the SMC appears to have a substantially more skew-symmetric magnitude distribution than that of the LMC. If we use the mean of the magnitudes of the red clump, we derive $\mu_{\mathrm{SMC}} \approx 18.76$, whereas if we use the mode, we derive $\mu_{\mathrm{SMC}} \approx 18.94$. It is only the latter that is consistent with the standard value of $\mu_{\mathrm{SMC}} = 18.95 \pm 0.07$, which is measured from the analysis of four eclipsing binary systems (Graczyk et al. 2014). An assessment of consistency in this case will thus require a much more detailed analysis of the color–magnitude diagram of the SMC.

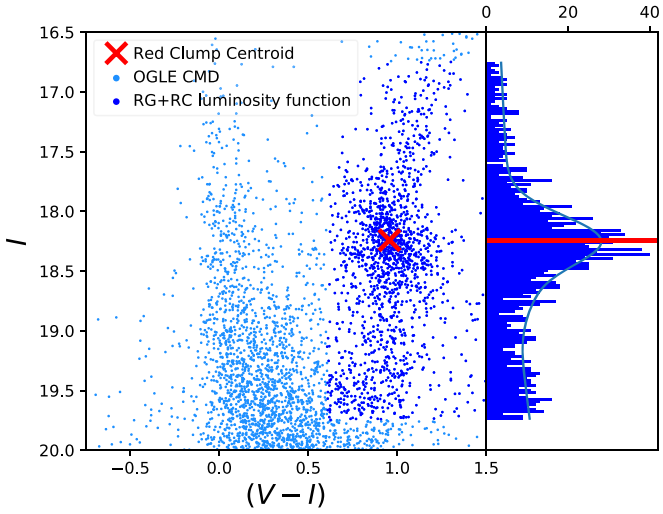

Figure 4. OGLE-III color–magnitude diagram and luminosity function of part of the field lmc100.1. The combination of intrinsic red clump properties estimated in this work, with its apparent properties estimated from the color–magnitude diagram, yields a distance modulus of $\mu_{\mathrm{LMC}} = 18.45 \pm 0.02$ (stat) $\pm$ 0.04(sys), consistent with the standard value of $\mu_{\mathrm{LMC}} = 18.48$ (Pietrzyński et al. 2019).

4. The Reddening toward the Magellanic Clouds

The Magellanic Clouds are among the best-studied sight lines in astronomy, and thus we have multiple options available to use independent tracers to test the available reddening maps derived from different choices for the color of the red clump. In this investigation, we use newly available observations of the colors of LMC Cepheids observed with HST, classical Cepheids observed from the ground, and RR Lyrae stars of the ab type observed from the ground.

4.1. Calibration with Cepheids

The intrinsic color of Cepheids can be estimated by means of well-calibrated period−color relations. They can then be treated as their own class of standard crayons, and thus the difference between their observed and intrinsic colors is an estimate of reddening. By comparing that estimate in the mean to the observed colors of red clump stars, we can estimate the intrinsic color of the latter.

We use two separate sets of data for this comparison. The first is that of 70 LMC Cepheids observed by Riess et al. (2019). These Cepheids have been observed in the WFC3-UVIS optical bands $F555W$ and $F814W$, in two HST programs, GO-14648 and GO-15146 (PI: Riess), across the inner part of the LMC. The color $(F555W - F814W)$ is similar to the $(V-I)$ color studied here to evaluate LMC reddening, We exclude two Cepheids, OGLE1940 and OGLE1945 with colors of 1.3 and 1.6 mag, 5σ and 8σ from the mean and indicative of high circumstellar reddening, which is distinct from the interstellar reddening measured by the maps. The advantage of this data is that HST provides unmatched resolution and stability to overcome errors in Cepheid photometry, which reside in some ground-based data due to crowding and zero-point variations in the LMC.

The second data set is that of 723 Cepheids from the catalog of Macri et al. (2015). That investigation used a combination of new infrared observations and optical *VI* photometry from the OGLE survey (Soszynski et al. 2008; Ulaczyk et al. 2013). The actual catalog of Macri et al. (2015) is larger than this sample—we restricted our analysis to Cepheids that were used in the final fit of that investigation and which were classified as fundamental rather than first-overtone pulsators. The advantages of this catalog relative to the HST one are that it is $\sim 10\times$ more numerous, and that it spans a $\sim 2\times$ larger area, including sight lines with slightly higher reddening.

We adopt two independent benchmarks for the unreddened Cepheid ($F555W-F814W$) period−color relations. The first is empirical, from Macri et al. (2006). They used HST data to study Cepheids in the nearby maser-host galaxy NGC 4258. Their sample includes 63 Cepheids with periods from 3 to 44 days toward an outer region, ∼20 kpc from the center of that face-on galaxy where the host reddening should be minimal. The mean metallicity of that region is similar to that of the LMC (Riess et al. 2016), as the outer region of NGC 4258 was shown to have a metallicity ∼0.3 dex below solar (Hoffmann et al. 2016), based on measurements of the $R23$ parameter in H II regions and presented on the Zaritsky et al. (1994) scale. The foreground reddening is also very low, $E(V-I)=0.022$, leaving little residual uncertainty after its removal. We note that the inclination angle toward this disk is $i=86.^{\circ}93\pm0.^{\circ}22$ (Humphreys et al. 2013), so nearly face on. We computed a weighted fit for a linear period−color relation to this data, which yields $(F555W-F814W)_0=(0.895\pm0.012)+(0.317\pm0.038)(\log[P/\mathrm{days}]-1)$.

The second unreddened benchmark is from the work of Fiorentino et al. (2013), who computed theoretical period −color relations from stellar pulsational models in the WFC3 $F555W-F814W$ system. Their predictions for various compositions can be found in their Table 1. We use the entry from that table that they recommend for the LMC, which is computed from stellar models with initial metals abundance $Z=0.008$ and initial helium abundance $Y=0.25$ and yields $(F555W-F814W)_0=0.90+0.31(\log[P/\mathrm{days}-1])$. That is consistent with that of the empirical relation within the errors of the latter.

In Figure 5, we plot the LMC Cepheid color ($F555W-F814W$) as observed versus log Period/days in the top panels. Then, in panels 2, 3, and 4, we show the derived dereddened colors of the Cepheids after using the reddening maps of Haschke et al. (2011), Górski et al. (2020), and Skowron et al. (2021). The left panels show the HST data (Riess et al. 2019), and the right panels show the scatter of the ground-based data (Macri et al. 2015). In each of the three panels, the reddening-free empirical period−color relation (Macri et al. 2006) is shown as the blue line, and the theoretical period−color relation (Fiorentino et al. 2013) is shown as the red line; both are quite similar.

Without dereddening, the observed period−color distribution lies at redder colors than the theoretical prediction of Fiorentino et al. (2013), by a mean of 0.054 mag in the ($F555W-F814W$) HST data, which approximately corresponds to 0.048 mag in $E(V-I)$, assuming $R_V=3.1$ (Fitzpatrick 1999). That is not surprising—the reddening toward the LMC is definitely greater than 0.

The application of reddening derived from Cepheids to the three red clump colors maps of Haschke et al. (2011), Górski et al. (2020), and Skowron et al. (2021) provide three pairs of estimates of $(V-I)_{RC,0}$ for each of the space-based and ground-based data. The three estimates will differ as the three maps have slightly different methodologies to measure the red clump color and slightly different resolutions. We take the mean of the three measurements as our derived value of $(V-I)_{RC,0}$. The error on $(V-I)_{RC,0}$ is the quadratic sum of the scatter in those three values and of the statistical error in the mean differences due to the scatter in the colors of the Cepheids. For the ground-based Cepheid data, we also incorporate a ∼0.02 mag error in the conversion from *VI* photometry to HST-UVIS photometry, identified by Riess et al. (2019).

Assuming the Fiorentino et al. (2013) relation, we derive $(V-I)_{RC,0,\mathrm{LMC}}=0.93\pm0.02$ from the HST data and $(V-I)_{RC,0,\mathrm{LMC}}=0.90\pm0.02$ from the ground-based data. If we assume the relation derived from the work of Macri et al. (2006), we derive $(V-I)_{RC,0,\mathrm{LMC}}=0.94\pm0.03$ from the HST data and $(V-I)_{RC,0,\mathrm{LMC}}=0.91\pm0.04$ from the ground-based data.

We comment on the possible origins of these differences. The first discrepancy is that the results derived from the relation of Macri et al. (2006) are ∼0.01 mag redder than the results derived from the Fiorentino et al. (2013) relation. That can be explained if, for example, the internal reddening of the outer field of NGC 4258 is not zero as we have assumed here, but $\langle E(V-I)\rangle=0.01$.

The second discrepancy is that the HST data lead to derived values of $(V-I)_{RC,0}$ that are ∼ 0.03 mag redder than those from the OGLE (ground-based) data. A partial contributor to this discrepancy has been identified by Riess et al. (2019): there is a 0.02 mag mean offset between directly measured space-based colors and space-based colors derived from ground-based colors. It is not clear if that offset is due to errors in the zero points, errors in the assumed filter transmission curves, or greater blending in the ground-based data. Separately, a granular analysis of the data suggests that 0.01 mag of the offset may be due to a statistical fluke. We find that dereddening the data using the maps of Skowron et al. (2021), with the analysis restricted to the period range that the two Cepheid samples have in common ($\log[P/\mathrm{days}]\geqslant 0.75$), yields a 0.01 mag offset in color if we use the same ground-based photometric colors for both.

Given these issues, we adopt the mean of the estimates from the ground-based sample and space-based samples, and assume the theoretical period−color relation as primary, for $(V-I)_{RC,0,\mathrm{LMC}}=0.914\pm0.02\approx0.91\pm0.02$.

4.2. Calibration with RR Lyrae (ab Type)

RR Lyrae stars are horizontal branch stars whose location in the Hertzsprung−Russell diagram places them in the instability strip. The relationship between their metallicities, pulsational periods, and $VIJHK_s$ magnitudes and colors are predicted by stellar theory (Catelan et al. 2004). There are many types of RR Lyrae stars; in this work, we use RR Lyrae of the ab type (hereafter denoted "RRab"). Population effects for RRab should not be large, as they probe a narrow region in the age −helium−metallicity phase space of stellar populations, typically only old ($\tau\gtrapprox 10$ Gyr) and metal-poor ([Fe/H] $\lesssim -1.0$) stars (Lee et al. 1994; Cassisi et al. 2004).

An RRab star's intrinsic color can be estimated from its pulsational properties and metallicity, which can be measured

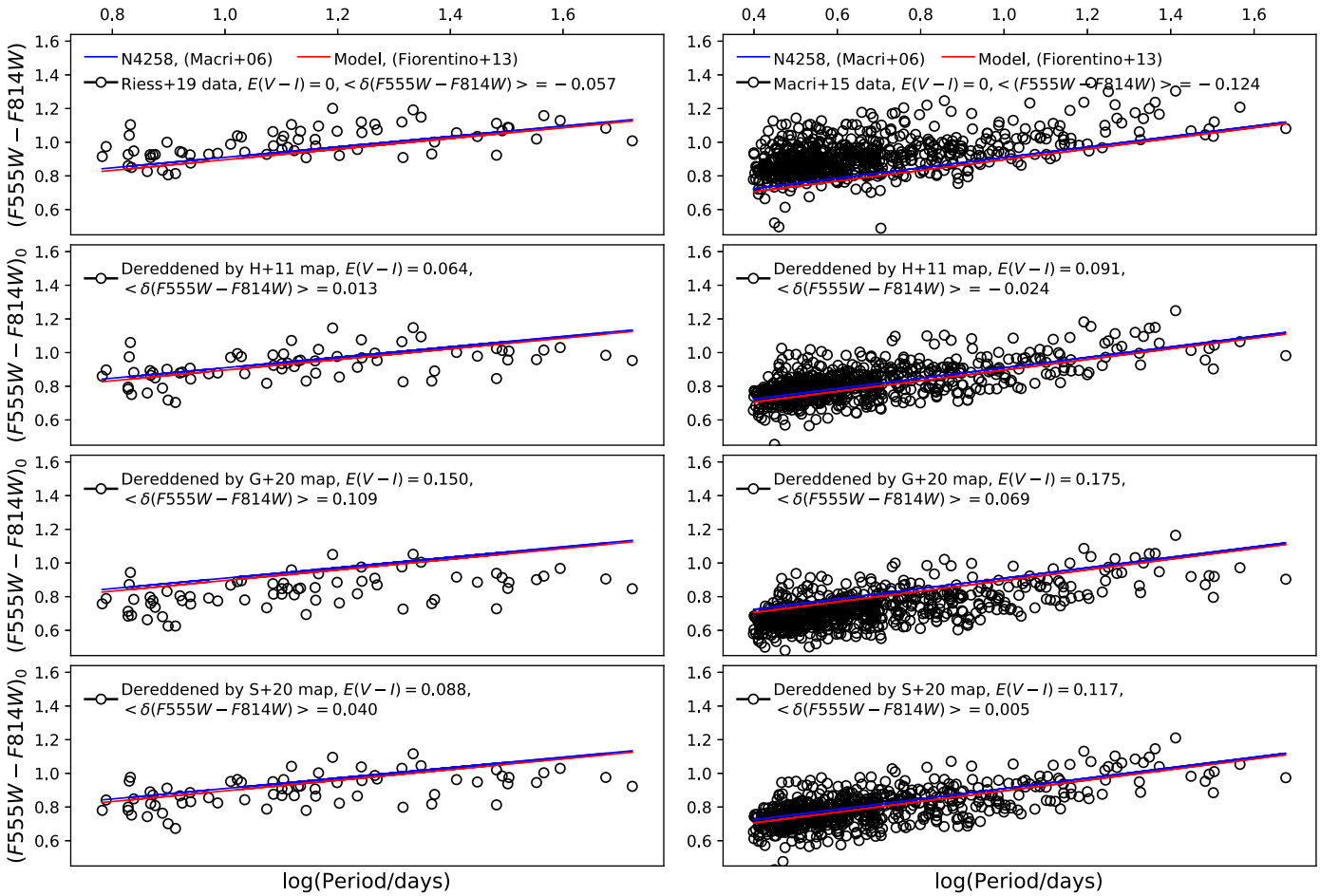

Figure 5. Comparison between the HST data (left column, Riess et al. 2019) and ground-based data (right column; Macri et al. 2015), with predicted period−color relations, under the assumption of no reddening (top tow), and three different reddening maps (bottom three rows). In the legends, the value of $\langle \delta(F555W - F814W) \rangle$ shows the mean excess of the Fiorentino et al. (2013) relation relative to that of the observations. In other words, a positive value suggests that the Cepheids have been too dereddened.

independently of distance and reddening. We use two different relationships. The first is the theory-derived, widely used (e.g., of Pietrukowicz et al. 2015; Kunder et al. 2016) relationship of Catelan et al. (2004):

$$(V-I)_{\mathrm{RRab},0} = 0.55 + 1.13\log(P/(0.60\ \mathrm{days})) + 0.070([\mathrm{Fe/H}] + 1.00) + 0.11([\mathrm{Fe/H}] + 1.00)^2, \quad (7)$$

where the models used by Catelan et al. (2004) assume that $\log Z = ([\mathrm{Fe/H}] - 1.765)$. We do not expect a perfect match with this model, as it reports synthetic colors for the RR Lyrae under the assumption that they are static stars, whereas the observational information that is available is that of $\langle V \rangle$ and $\langle I \rangle$, which are intensity-weighted mean magnitudes. We could not find predictions for the offset between $(V-I)_{\mathrm{Static}}$ and $\langle V \rangle - \langle I \rangle$, but the classic work of Bono et al. (1995) suggests that the synthetic $(B-V)_s$ color should be between 0.00 and 0.07 mag redder than the difference between the intensity-weighted magnitudes, $\langle B \rangle$ and $\langle V \rangle$.

The second relationship is empirical, which we derive from the compilation of Monson et al. (2017), using reddening corrections from Neeley et al. (2019), restricting the sample to those stars satisfying $E(V-I) = 1.40E(B-V) \leqslant 0.10$ ($R_V = 3.1$, Fitzpatrick 1999):

$$(\langle V \rangle - \langle I \rangle)_{\mathrm{RRab},0} = 0.49 + 0.69\log(\mathrm{P}/(0.60\ \mathrm{days})) + 0.043([\mathrm{Fe/H}] + 1.00), \quad (8)$$

where the metallicities are taken from the work of Fernley & Barnes (1997), and the colors are the differences in the intensity-mean magnitudes. The reddening cut of $E(V-I) = 1.40E(B-V) \leqslant 0.10$ is implemented as the higher-reddening values are almost certainly overestimates. The correlation between dereddened color and reddening, if all RRabs are included, is given by $\rho = -0.36$ with a p value of 0.03.

The calibration provided by Equation (8) enables us to use the RRab stars in the LMC and SMC as standard crayons. We can compare the $E(V-I)$ derived from RRab stars to the $(V-I)_{RC}$ measured by Górski et al. (2020) and Skowron et al. (2021) to calibrate the zero-point for the latter.

The LMC and SMC RR Lyrae are taken from the catalog of Soszyński et al. (2016), from which we used the subsample analyzed by Skowron et al. (2016), which is selected to have more secure lightcurves and more secure metallicities derived from the Fourier components of the lightcurves. That sample totals 24,133 LMC and SMC RRab stars with OGLE-IV lightcurves. We use

the metallicities that are on the Jurcsik (1995) scale, for which Skowron et al. (2016) estimate the typical error to be 0.10 dex. We then restrict the analysis to RRab stars with $(V-I)_{\rm Observed} \geqslant 0.35$, $-1.75 \leqslant [{\rm Fe/H}]_{\rm Fourier} \leqslant -0.25$, and $0.45 \leqslant P/{\rm days} \leqslant 0.80$. That leaves a sample of 16,333 LMC RRab stars, and 1612 SMC RRab stars.

We compare the RRab-derived reddening maps to the RC-derived maps as follows. We restrict the comparison to the grid elements in the maps of Górski et al. (2020) that satisfy $\sigma_{V-I,RC} \leqslant 0.06$ and $E(V-I)_{RC} \leqslant 0.40$ to reduce the confounding effects of high reddening and differential reddening. The mean separation to the centers of the LMC and SMC are 2.°6 and 1.°6, respectively. Similarly, for the grid of Skowron et al. (2021), we require $\sigma_{V-I,RC} \leqslant 0.05$ and $E(V-I)_{RC} \leqslant 0.40$. The mean separation to the centers of the LMC and SMC are 3.°4 and 1.°2, respectively. Then, for each grid element, we keep those with at least two RRab stars, and we take the mean derived reddening difference between the RRab stars and the RC value in that grid element. We then take the median of the comparisons for all of the grid points.

For the LMC, using the grid of Górski et al. (2020), we derive $(V-I)_{RC,0} = 0.95$ and $(V-I)_{RC,0} = 0.89$ by assuming the intrinsic (dereddened) RRab colors as derivable from Equations (7) and (8). Similarly, if we use the grid of Skowron et al. (2021), we derive $(V-I)_{RC,0} = 0.96$ and $(V-I)_{RC,0} = 0.89$ using Equations (7) and (8). We choose the latter results from Equation (8) as the primary, as it is calibrated off of the same class of colors as it measures, the difference between intensity-weighted magnitudes. For both relationships, the median absolute deviation was 0.03 mag. The standard deviation, using Equation (8), when removing outlier pixels with $\delta E(V-I) \geqslant 0.15$ mag is ∼0.05 mag.

For the SMC, we repeat the exercise with one adjustment: we require only one RRab star per grid element, as the density of RRab stars with reliable parameters in that population appears to be lower. Using the grid of Górski et al. (2020), we derive $(V-I)_{RC,0} = 0.89$ and $(V-I)_{RC,0} = 0.82$ by assuming the intrinsic (dereddened) RRab colors as derivable from Equations (7) and (8). Similarly, if we use the grid of Skowron et al. (2021), we derive $(V-I)_{RC,0} = 0.95$ and $(V-I)_{RC,0} = 0.87$ using Equations (7) and (8). The standard deviation, using Equation (8), when removing outlier pixels with $\delta E(V-I) \geqslant 0.15$ mag is ≈0.06 mag.

For both the LMC and the SMC, the scatter between $E(V-I)_{\rm RC}$ and $E(V-I)_{\rm RRab}$ is larger than that of the fit to Equation (8), of $\delta = 0.026$ mag. This can be explained if there is some combination of a little differential reddening ($\delta E(V-I) \approx 0.05$) in each field, if the scatter to Equation (8) is underestimated by the small or perhaps nonrepresentative local sample or if the best-fit parameters to Equation (8) are slightly off. The last possibility is explored in the next subsection.

4.2.1. Uncertainties in the Calibration with RR Lyrae (ab Type)

The scatter in the color of the 24 RRab stars from the mean relation of Equation (8) is given by $\delta = 0.026$ mag. The errors in the three coefficients are 10^{-2} (0.97, 10, 1.2), and the correlation matrix for the uncertainties is given by

$$Corr = \begin{pmatrix} 1 & 0.80 & 0.66 \\ 0.80 & 1 & 0.67 \\ 0.66 & 0.67 & 1 \end{pmatrix}.$$

The uncertainty due to the zero point is given as 0.0097 mag. The uncertainty in the determinations of the individual periods negligibly contributes to that for individual RRab, whose periods are typically determined to 1 part in 100,000. The mean effect will be much larger, as the mean value of $\log(P/(0.60\ {\rm days}))$ for the Monson et al. (2017) sample and the LMC and SMC sample differs by 0.047 and 0.059, respectively, with the latter RRab populations having, on average, longer periods. The differences in the metallicities of the LMC and SMC with respect to the sample of Monson et al. (2017) are 0.21 ± 0.20 and 0.59 ± 0.08, with the LMC and SMC RRab stars having lower metallicities (Skowron et al. 2016).

The relationship of Equation (8) necessitates a zero-point shift in the reddening maps of Górski et al. (2020), to $(V-I)_{\rm RC,0,LMC} \approx 0.89 \pm 0.02$ and $(V-I)_{\rm RC,0,SMC} \approx 0.82 \pm 0.02$. If we repeat the exercise with the reddening maps of Skowron et al. (2021), we derive $(V-I)_{\rm RC,0,LMC} \approx 0.89 \pm 0.02$ and $(V-I)_{\rm RC,0,SMC} \approx 0.87 \pm 0.02$. As the differences here are likely due to a combination of the different resolutions and different locations of the boundaries of each grid point, we adopt the average of these results as primary.

4.3. Implications for the Reddening of the Tip of the Red Giant Branch in the LMC

The TRGB is a primary distance indicator that is commonly used to measure the distance to galaxies by tracing the stellar population in their halos where extinction is minimal. Because the TRGB is not a type of star but rather the maximum luminosity of many red giants, it is difficult to calibrate this luminosity without reliable parallaxes for a large number of red giants near the tip (Mould et al. 2019). Instead, the TRGB is most commonly calibrated in the LMC using its measured distance. Unfortunately, TRGB stars in the LMC suffer substantial extinction in the I band, and thus, the calibration of TRGB in the halos depends directly on the estimate of the absolute (i.e., true, not differential) LMC extinction or reddening. Here we consider the estimate of the LMC TRGB extinction in light of the red clump calibration from Section 2.

The reddening maps from Haschke et al. (2011) yield a mean value of $A_I = 0.10$ (mag) for the sight lines of stars near the TRGB as determined by Jang & Lee (2017a, 2017b) and Yuan et al. (2019) which were derived from a value of $(V-I)_{RC,0} = 0.92$, consistent with the values found here. This extinction calibration leads to $M_{I,TRGB} = -3.97 \pm 0.03$ based on the detached eclipsing binary distance to the LMC of $m-M = 18.477$ (Pietrzyński et al. 2019) and an apparent $m_{I,TRGB} = 14.60$.

For an independent comparison, we measured the extinction of TRGB sight lines from LMC reddening maps derived from RR Lyrae star colors. RR Lyrae should provide very good tracers for TRGB extinction as they are similar in age and are good calibrated crayons. We measured the median reddening of the TRGB sight lines (TRGB samples from Jang & Lee (2017a, 2017b) and Yuan et al. (2019)) using the RR Lyrae LMC reddening maps discussed in Section 4.2 and find a median value of $A_I = 0.16$ and $A_I = 0.08$ mag using the Monson et al. (2017) and Catelan et al. (2004) relationships, respectively. These results match well those from the Haschke et al. (2011) red clump maps, but see further discussion in Section 5.

Table 4
Summary of the Estimates for the Intrinsic Colors of the LMC and SMC Red Clumps from the Different Methods Explored in This Work

Method	$(V-I)_{\rm RC,0,LMC}$	$\langle\delta\psi\rangle$	$(V-I)_{\rm RC,0,SMC}$	$\langle\delta\psi\rangle$
BaSTI v1 isochrones no empirically derived offsets	≈ 0.92	2.8	≈ 0.87	1.6
BaSTI v1 isochrones with empirically derived offsets	≈ 0.90	2.8	≈ 0.85	1.6
BaSTI v1 " plus composite population effects	≈ 0.93	2.8	⋯	1.6
HST-observed Cepheids assuming an empirical color−period relation	0.94 ± 0.03	1.4	⋯	⋯
HST-observed Cepheids assuming a theoretical color−period relation	0.93 ± 0.02	1.4	⋯	⋯
OGLE-observed Cepheids assuming an empirical color−period relation	0.91 ± 0.04	1.2	⋯	⋯
OGLE-observed Cepheids assuming a theoretical color−period relation	0.90 ± 0.02	1.2	⋯	⋯
RRab assuming an empirical period−color relation	0.89 ± 0.02	3.0	0.84 ± 0.02	1.4

Note. The variable $\langle\delta\psi\rangle$ denotes the mean angular separation in degrees between the center of the host galaxy and the coordinates of the sources contributing to the measurement. In this work, we assume LMC and SMC centers of (α,δ)=(05:23:35, −69:45:22) and (00:52:38, −72:48:01).

5. Discussion

We sought to estimate the intrinsic color, $(V-I)_{RC,0}$, of the red clumps of the Magellanic Clouds. Using predictions from (i) the BaSTI isochrones shifted by an offset calibrated off of three stellar populations, (ii) the Cepheids period−color relations, and (iii) the RR Lyrae period−color relations, we have estimated that $(V-I)_{RC,0,\rm LMC} = \{\approx 0.93,\ 0.91 \pm 0.02,\ 0.89 \pm 0.02\}$, respectively, and using the first and third methods, that $(V-I)_{RC,0,\rm SMC} = \{\approx 0.85,\ 0.84 \pm 0.02\}$, respectively. A summary of the different methods is listed in Table 4. In pursuit of that goal, we have also demonstrated the following:

1. The offset between the predictions of the BaSTI v1 isochrones with Reimers' mass-loss parameter $\eta = 0.20$ and the observations of red clump stars is remarkably consistent over a broad metallicity interval. The offset is given by $\Delta(V-I)_{RC,0},\ \Delta M_{I,RC} = (0.02 \pm 0.01,\ 0.13 \pm 0.03)$, with the observations being redder and fainter than the theoretical predictions. That $\Delta(V-I)_{RC,0}$ is smaller than $\Delta M_{I,RC}$ is consistent with the finding of Salaris et al. (2016), who estimated, using the same stellar evolution code, an upper bound on the mass lost by red giant star progenitors in 47 Tuc of $\Delta M \approx 0.17 M_{\odot}$, some 70% larger than that predicted when assuming $\eta = 0.20$. The predictions of the updated BaSTI database, BaSTI version 2.0, are both consistent with zero. In passing, this represents sound evidence of the reliability and accuracy of the physical framework adopted for the new version of the BaSTI model library.
2. The different calibrations yield results that are remarkably consistent with each other. For the LMC Cepheid sample, the theoretically calibrated period–color relation of Fiorentino et al. (2013) is consistent with the empirically calibrated relation from Macri et al. (2006), from which the derived reddening estimates are consistent with those obtained using the RR Lyrae.

That is an impressive degree of consistency. It is also the case that reddening maps derived from observations of RR Lyrae need not perfectly agree with reddening maps derived from observations of red clump stars—the former are a more metal-poor population and thus likely kinematically hotter. They may have a different spatial distribution with respect to the dust.

One calibration that is not consistent with that used in this work is the one used by Górski et al. (2020). They estimated the reddening along different sight lines using the blue supergiant sample of Urbaneja et al. (2017) as standard crayons. A plausible explanation for this is that the blue supergiants with ages of ∼1 Myr are along sight lines with extinction greater than the mean value probed by the ∼3′, corresponding to approximately 44 pc, the resolution of the reddening maps of Górski et al. (2020). Indeed, the mean value of $R_V = A_V/E(B-V)$ toward the blue supergiants is $\langle R_V\rangle = 4.5$. That is not consistent with the standard value of $R_V = 3.1$. If, for example, the reddening toward the blue supergiants is due to two components of extinction, one with $R_V = 3.1$ and another with $R_V = 6$, then the $R_V = 3.1$ component, which is the only component that contributes to the red clump stars, accounts for approximately half of the extinction to the blue supergiants. Further, given that the mean error on R_V is also approximately equal to the standard deviation in the derived R_V values, it may be that all of the blue supergiants in the sample have this extra extinction along their line of sight.

Similarly, the fact that the reddening estimates toward Cepheids are consistent with those toward red clump stars and RR Lyrae indicates that there is null or negligible extra extinction toward Cepheids. Whatever extra extinction there is, is likely to exist toward younger stars of $t \sim 1$ Myr, it is significantly reduced or eliminated by the time those stars are ∼100 Myr old, the typical age of Cepheids (Bono et al. 2005). For example, the study of Anderson & Riess (2018) showed that ∼98% of the Cepheids in the Andromeda galaxy have migrated away from their dusty birth sites. Because cluster disruption times are generally longer than blue supergiant ages, it is reasonable to assume that the additional extinction for blue supergiants comes from their birth sites.

Skowron et al. (2021) derived reddening maps for the Magellanic Clouds by dereddening red clump star colors in the outskirts of the Clouds (3°–9° and 1°–4° away for the LMC and SMC, respectively) where the Schlegel et al. maps (1998) should give more valid results. They then corrected for the metallicity dependence of the color of the red clump to derive intrinsic red clump colors of $(V-I)_{RC,0,\rm LMC} = 0.8915 - d \times 0.0025$, and $(V-I)_{RC,0,\rm SMC} = 0.8816 \pm 0.0112$ for $d \leqslant 1\overset{\circ}{.}5$, and $(V-I)_{RC,0,\rm SMC} = 0.8667 \pm 0.0031$ for $d > 1.5$

Freedman et al. (2020) present a method to measure the reddening of TRGB stars in the LMC that does not appear to agree with the LMC reddening maps previously discussed. They simultaneously measured the difference in distance and reddening between the LMC and another host using the colors

of their respective TRGBs, e.g., in the SMC and LMC:

$$\Delta\mu(\mathrm{SMC}-\mathrm{LMC}) = (m_{x,\mathrm{SMC}} - R(x,I)A_{I,SMC}) - (m_{x,\mathrm{LMC}} - R(x,I)A_{I,\mathrm{LMC}}), \quad (9)$$

where $m_{x,\mathrm{SMC}}$ is the apparent magnitude of TRGB in one of five bands (V, I, J, H, K_s), and $R(x, I)$ is the ratio of extinction between band x and I. They estimate $A_{I,\mathrm{SMC}}$ from the Galactic foreground reddening maps of Schlafly & Finkbeiner (2011) as given in NED, then solve for two parameters, $\Delta\mu$ and $A_{I,\mathrm{LMC}}$. They find a significantly higher value of $A_I = 0.169 \pm 0.02$, $>3\sigma$ higher than the value derived from the red clump star map of Haschke et al. (2011) However, an apparent discrepancy in measurements of the TRGB $m_{I,\mathrm{SMC}}$ might explain this difference.

Freedman et al. (2020) report a value of SMC TRGB $m_{I,\mathrm{SMC}} = 14.93 \pm 0.01$ from OGLE photometry. Górski et al. (2016) found the SMC TRGB from OGLE photometry is broad and brighter and varies across five SMC fields from 14.98 to 15.20 with a mean of m_I=15.04. Yuan et al. (2019) found m_I = 15.01 from the OGLE data, consistent with Górski et al. (2016) but also fainter than Freedman et al. (2020) by ~0.1 mag. As shown in Equation (9), $m_{I,\mathrm{SMC}} + A_{I,\mathrm{LMC}} \sim \Delta\mu$ so a higher value of $m_{I,\mathrm{SMC}}$ by ~0.1 mag than Freedman et al. (2020) yields a lower value of $A_{I,\mathrm{LMC}}$ by this difference for the same $\Delta\mu$ ($\Delta\mu$ is well constrained in the measured range by the relative detached eclipsing binary distance from Wielgórski et al. 2017 with $\sigma = 0.026$ mag) and could explain the discrepancy with the LMC reddening maps. Freedman et al. (2020) does not indicate which stars in the SMC (or LMC) OGLE catalogs (i.e., the region, magnitude range, or filtering characteristics) were employed to measure the TRGB so we cannot readily resolve or reproduce the differences in $m_{I,\mathrm{SMC}}$ with Górski et al. (2016) or Yuan et al. (2019).

Another source of discrepancy is the foreground estimate of $A_{I,\mathrm{SMC}}$ used by Freedman et al. (2020) via NED. This value is quite uncertain because it cannot be derived directly from the IRAS maps (Neugebauer et al. 1984) used by Schlafly & Finkbeiner (2011) because the Magellanic Clouds contaminate the foreground glow. One may interpolate the IRAS maps around the ~10° perimeter of the SMC where the maps show $\sigma \sim E(B-V) \sim 0.015$ mag (the Magellanic Stream also provides regional contamination of the IRAS maps) resulting in an uncertainty of $A_{V,\mathrm{SMC}}$ of 0.05 mag, which lowers the precision of the TRGB method considerably. In addition, the large range in the SMC TRGB values may result from a large depth (Subramanian & Subramaniam 2012), which also challenges the precision of the SMC to LMC comparison. An independent comparison between the LMC and IC 1613 (old, dwarf elliptical) by Freedman et al. (2020) avoids the issues with the SMC but the metallicities and ages of the TRGB span a larger range of 1 dex and systematic differences in TRGB may arise. Freedman et al. (2020) account for age and metallicity differences with a linear color term, but there is empirical evidence that this may not fully rectify the disparity; there is excessive dispersion beyond the quoted 0.01 mag TRGB errors between hosts as the χ^2 for the color comparison (Equation (9) for the LMC-IC 1613 comparison) is 16 for 3 degrees of freedom ($P = 0.1\%$). Whether the high value of χ^2 is due to higher measurement errors or intrinsic variation in color-corrected TRGB colors (see McQuinn et al. (2019)) , the uncertainty in $A_{I,\mathrm{LMC}}$ would be higher by $\sim\sqrt{(}5)$.

Could the sight lines of TRGB in the LMC have much higher extinction than red clump or RR Lyrae tracers? In principle, red clump and RR Lyrae stars should provide good measures of dust sight lines for near-TRGB stars as they are all highly evolved red giants of ⩾Gyr timescales. In general, older populations have more time to migrate from their dusty star-forming birth sites so a hierarchy of ages would correspond to a hierarchy of extinction. As shown in Section 4.1, the red clump star maps of Haschke et al. (2011) agree with the colors of Cepheids, which are even younger (at 50–100 Myr) than the red clump stars. TRGB stars should be a slightly older population (an older stellar population produces fewer horizontal branches and particularly fewer red clump stars per capita, and correspondingly, more red giant stars), so it is unlikely TRGB stars would have statistically more extinction than red clump stars and Cepheids. Freedman et al. (2020) and Joshi & Panchal (2019) identify a range of recent LMC literature values of A_I of 0.10 to 0.20 mag measured from B stars, red clump stars, RR Lyrae, star clusters, Cepheids, and detached eclipsing binary stars. The Freedman et al. (2020) value of $A_I = 0.17$ mag falls at the higher end of this range and the value of $A_I = 0.10$ mag from the Haschke et al. (2011) maps at the lower end. Because all of these stellar tracers are younger and likely along dustier sight lines than TRGB stars (with the exception of RR Lyrae), considering the range and age of the population, TRGB stars would seem likely to fall at the low end of this range.

An attractive alternative to estimating the extinction of TRGB in the LMC is to calibrate it in the halo of the maser host NGC 4258 (Jang & Lee 2017a; Reid et al. 2019) where the result, like the application in Type Ia supernova hosts, is insensitive to dust.

5.1. Prospects for Further Work

Additional and independent estimates of the reddening toward the Magellanic Clouds would be useful not just to simply further calibrate the latter, but alternatively, to explore the consistency of different approaches. Among the possibilities:

1. To compare the predictions for the red clump of the BaSTI isochrones, either of version 1 or version 2, with a larger sample of robust empirical anchors. We would have liked to do so, but most of the metal-rich clusters are toward the inner Milky Way and thus have nonstandard extinction along their lines of sight (Nishiyama et al. 2008; Nataf et al. 2016). Separately, the horizontal branch morphologies of globular clusters are sensitive to variations in the initial abundances of helium (Busso et al. 2007; Dotter et al. 2010; Milone et al. 2014; Marino et al. 2014). The latter are not always as well determined as they are for 47 Tuc.
2. To measure the foreground reddening toward the Magellanic Clouds using both a probabilistic analysis of the spectroscopic, photometric, and parallax information of foreground stars in GALAH (De Silva et al. 2015), as well as the measurements of the equivalent widths of the diffuse interstellar bands in their spectra. We could not do so here as the reddening estimates are not in the most up-to-date publicly available data release (Buder et al. 2019). We did attempt to do this with APOGEE data, from

which we estimated the foreground $A_I \approx 0.12$, but that sample was of only ~30 stars.

3. To measure additional colors of the red clump to break the degeneracy between reddening variations and intrinsic color variations. We attempted to do this with the $(g-i)$ measurements of Choi et al. (2018), but this did not yield a robust constraint as $E(g-i)/E(V-I)$ has approximately the same value as the $\delta(g-i)/\delta(V-I)$ that results from variations in stellar effective temperature. In contrast, with infrared data, $E(I-K_s)/E(V-I) \approx 1.04$, and $\delta(I-K_s)/\delta(V-I) \approx 0.47$.
4. To use open and globular clusters in the Magellanic Clouds as standard crayons. At this time, that literature is very heterogeneous in its assumptions (choice of isochrones, rotation rates, etc.) and thus the resultant reddening scale ends up being subjective. Further, many of the clusters have photometric metallicity estimates, for which the derivation is degenerate with that of the reddening.
5. To obtain spectroscopic [Fe/H] and hopefully [α/Fe] measurements for a larger number of solar neighborhood RR Lyrae. The correlations in the errors to the terms of Equation (8) are all large and positive, +0.66, + 0.67, and + 0.80. These could be reduced, and better understand, with a larger sample of RR Lyrae stars with robustly determined metallicities. Ideally, some LMC and SMC RR Lyrae would have their spectroscopic abundances measured in a consistent manner with those of the solar neighborhood. An investigation of the difference between static magnitudes, time-weighted mean magnitudes, and intensity-weighted mean magnitudes of RR Lyrae for every bandpass would also be beneficial.

6. Conclusion

In this investigation, we have investigated three different methods to estimate the intrinsic color, $(V-I)_{RC,0}$, of the red clumps of the inner few degrees of the Magellanic Clouds.

The first method was derived from the predictions of the BaSTI version 1 isochrones, for which we applied empirically calibrated offsets calibrated by comparing the isochrone predictions to the observations of the globular cluster 47 Tuc, the solar neighborhood, and the open cluster NGC 6791. Together, these three populations constitute a robust calibration set, as they span a metallicity range of Δ[Fe/H] ≈ 1.1 dex. The BaSTI isochrones predict red clumps that are slightly red and bright relative to the observations, by $\Delta(V-I)_{RC,0}$, $\Delta M_{I,RC} \approx (0.02, 0.13)$, with these offsets being almost equal to the offsets between the BaSTI version 1 and version 2 isochrones. We applied this offset to calculate our first estimate of the red clumps of the Magellanic Clouds and obtained $(V-I)_{RC,0,\mathrm{LMC}} = 0.93$ and $(V-I)_{RC,0,\mathrm{SMC}} = 0.85$, and also $M_{I,RC,\mathrm{LMC}} \approx -0.26$ and $M_{I,RC,\mathrm{SMC}} \approx -0.37$.

The second method derived estimates by comparing the reddening toward Cepheids, for which we assumed that the average intrinsic colors can be reliably determined from the period–color relations, with the reddening values estimated from the nearest red clump centroid measurement. The estimate was nearly the same regardless of whether or not we used the empirically calibrated period–color relation of Macri et al. (2006) or the theoretically derived period–color relation of Fiorentino et al. (2013). The resulting estimate was $(V-I)_{RC,0,\mathrm{LMC}} = 0.91 \pm 0.02$.

The third method derived estimates by using the OGLE RR Lyrae catalog of Soszyński et al. (2016), with metallicity estimates from Skowron et al. (2016) as a set of standard crayons with which to estimate the reddening along their lines of sight. The $(V-I)_{\mathrm{RRab}}$ colors predicted by the empirically calibrated period–color relation from the data of Monson et al. (2017) yield the estimates $(V-I)_{RC,0,\mathrm{LMC}} = 0.89 \pm 0.02$ and $(V-I)_{RC,0,\mathrm{SMC}} = 0.84 \pm 0.02$.

We thank the referee for helpful feedback on the manuscript.

We thank Aaron Dotter, Adriano Pietrinferni, Dan Scolnic, Andrea Kunder, Marcio Catelan, Dan Weisz, Marek Gorski, and Dorota Skowron for helpful discussion.

D.M.N. acknowledges support from NASA under award number 80NSSC19K0589, and support from the Allan C. And Dorothy H.Davis Fellowship. S.C. acknowledges support from Premiale INAF MITiC, from Istituto Nazionale di Fisica Nucleare (INFN; Iniziativa specifica TAsP), and grant AYA2013-42781P from the Ministry of Economy and Competitiveness of Spain. L.C. acknowledges support from the Australian Research Council Future Fellowship FT160100402.

This work has made use of data from the European Space Agency (ESA) mission Gaia (https://www.cosmos.esa.int/gaia), processed by the Gaia Data Processing and Analysis Consortium (DPAC, https://www.cosmos.esa.int/web/gaia/dpac/consortium). Funding for the DPAC has been provided by national institutions, in particular the institutions participating in the Gaia Multilateral Agreement.

This publication makes use of data products from the Two Micron All Sky Survey, which is a joint project of the University of Massachusetts and the Infrared Processing and Analysis Center/California Institute of Technology, funded by the National Aeronautics and Space Administration and the National Science Foundation.

Funding for the Sloan Digital Sky Survey IV has been provided by the Alfred P. Sloan Foundation, the U.S. Department of Energy Office of Science, and the Participating Institutions. SDSS-IV acknowledges support and resources from the Center for High-Performance Computing at the University of Utah. The SDSS website is www.sdss.org. SDSS-IV is managed by the Astrophysical Research Consortium for the Participating Institutions of the SDSS Collaboration including the Brazilian Participation Group, the Carnegie Institution for Science, Carnegie Mellon University, the Chilean Participation Group, the French Participation Group, Harvard-Smithsonian Center for Astrophysics, Instituto de Astrofísica de Canarias, The Johns Hopkins University, Kavli Institute for the Physics and Mathematics of the Universe (IPMU)/University of Tokyo, the Korean Participation Group, Lawrence Berkeley National Laboratory, Leibniz Institut für Astrophysik Potsdam (AIP), Max-Planck-Institut für Astronomie (MPIA Heidelberg), Max-Planck-Institut für Astrophysik (MPA Garching), Max-Planck-Institut für Extraterrestrische Physik (MPE), National Astronomical Observatories of China, New Mexico State University, New York University, University of Notre Dame, Observatário Nacional/MCTI, The Ohio State University, Pennsylvania State University, Shanghai Astronomical Observatory, United Kingdom Participation Group, Universidad Nacional Autónoma de México,

University of Arizona, University of Colorado Boulder, University of Oxford, University of Portsmouth, University of Utah, University of Virginia, University of Washington, University of Wisconsin, Vanderbilt University, and Yale University.

ORCID iDs

David M. Nataf https://orcid.org/0000-0001-5825-4431
Santi Cassisi https://orcid.org/0000-0001-5870-3735
Luca Casagrande https://orcid.org/0000-0003-2688-7511
Wenlong Yuan https://orcid.org/0000-0001-9420-6525
Adam G. Riess https://orcid.org/0000-0002-6124-1196

References

An, D., Terndrup, D. M., Pinsonneault, M. H., & Lee, J.-W. 2015, ApJ, 811, 46
Anderson, R. I., & Riess, A. G. 2018, ApJ, 861, 36
Anthony-Twarog, B. J., Twarog, B. A., & Mayer, L. 2007, AJ, 133, 1585
Bailer-Jones, C. A. L., Rybizki, J., Fouesneau, M., Mantelet, G., & Andrae, R. 2018, AJ, 156, 58
Baumgardt, H., Hilker, M., Sollima, A., & Bellini, A. 2019, MNRAS, 482, 5138
Bergbusch, P. A., & Stetson, P. B. 2009, AJ, 138, 1455
Blanton, M. R., Bershady, M. A., Abolfathi, B., et al. 2017, AJ, 154, 28
Boesgaard, A. M., Lum, M. G., & Deliyannis, C. P. 2015, ApJ, 799, 202
Bono, G., Caputo, F., & Stellingwerf, R. F. 1995, ApJS, 99, 263
Bono, G., Marconi, M., Cassisi, S., et al. 2005, ApJ, 621, 966
Bovy, J., Nidever, D. L., Rix, H.-W., et al. 2014, ApJ, 790, 127
Bressan, A., Marigo, P., Girardi, L., et al. 2012, MNRAS, 427, 127
Brogaard, K., VandenBerg, D. A., Bruntt, H., et al. 2012, A&A, 543, A106
Buder, S., Lind, K., Ness, M. K., et al. 2019, A&A, 624, A19
Busso, G., Cassisi, S., Piotto, G., et al. 2007, A&A, 474, 105
Caffau, E., Ludwig, H. G., Steffen, M., Freytag, B., & Bonifacio, P. 2011, SoPh, 268, 255
Carrell, K., Wilhelm, R., & Chen, Y. 2012, AJ, 144, 18
Carrera, R., Gallart, C., Hardy, E., Aparicio, A., & Zinn, R. 2008, AJ, 135, 836
Casagrande, L., & VandenBerg, D. A. 2014, MNRAS, 444, 392
Cassisi, S., Castellani, M., Caputo, F., & Castellani, V. 2004, A&A, 426, 641
Cassisi, S., Potekhin, A. Y., Pietrinferni, A., Catelan, M., & Salaris, M. 2007, ApJ, 661, 1094
Catelan, M., Pritzl, B. J., & Smith, H. A. 2004, ApJS, 154, 633
Chan, V. C., & Bovy, J. 2020, MNRAS, 493, 4367
Chen, Y., Bressan, A., Girardi, L., et al. 2015, MNRAS, 452, 1068
Chen, Y., Girardi, L., Bressan, A., et al. 2014, MNRAS, 444, 2525
Chen, Y. Q., Casagrande, L., Zhao, G., et al. 2017, ApJ, 840, 77
Choi, J., Dotter, A., Conroy, C., et al. 2016, ApJ, 823, 102
Choi, Y., Nidever, D. L., Olsen, K., et al. 2018, ApJ, 866, 90
Cohen, R. E., Kalirai, J. S., Gilbert, K. M., et al. 2018, AJ, 156, 230
Cordier, D., Pietrinferni, A., Cassisi, S., & Salaris, M. 2007, AJ, 133, 468
Correnti, M., Bellazzini, M., Ibata, R. A., Ferraro, F. R., & Varghese, A. 2010, ApJ, 721, 329
De Silva, G. M., Freeman, K. C., Bland-Hawthorn, J., et al. 2015, MNRAS, 449, 2604
di Criscienzo, M., Ventura, P., D'Antona, F., Milone, A., & Piotto, G. 2010, MNRAS, 408, 999
Dolphin, A. E. 2002, MNRAS, 332, 91
Donor, J., Frinchaboy, P. M., Cunha, K., et al. 2018, AJ, 156, 142
Dotter, A. 2016, ApJS, 222, 8
Dotter, A., Sarajedini, A., Anderson, J., et al. 2010, ApJ, 708, 698
Ferguson, J. W., Alexander, D. R., Allard, F., et al. 2005, ApJ, 623, 585
Fernley, J., & Barnes, T. G. 1997, A&AS, 125, 313
Feuillet, D. K., Frankel, N., Lind, K., et al. 2019, MNRAS, 489, 1742
Fiorentino, G., Musella, I., & Marconi, M. 2013, MNRAS, 434, 2866
Fitzpatrick, E. L. 1999, PASP, 111, 63
Flewelling, H. A., Magnier, E. A., Chambers, K. C., et al. 2020, ApJS, 251, 7
Freedman, W. L., Madore, B. F., Hoyt, T., et al. 2020, ApJ, 891, 57
Gaia Collaboration, Prusti, T., & de Bruijne, J. H. J. 2016, A&A, 595, A1
García-Berro, E., Torres, S., Althaus, L. r. G., et al. 2010, Natur, 465, 194
García Pérez, A. E., Allende Prieto, C., Holtzman, J. A., et al. 2016, AJ, 151, 144
Gilmozzi, R., & Spyromilio, J. 2007, Msngr, 127, 11
Girardi, L. 2016, ARA&A, 54, 95
Girardi, L., & Salaris, M. 2001, MNRAS, 323, 109
Górski, M., Pietrzyński, G., Gieren, W., et al. 2016, AJ, 151, 167
Górski, M., Zgirski, B., Pietrzyński, G., et al. 2020, ApJ, 889, 179
Graczyk, D., Pietrzyński, G., Thompson, I. B., et al. 2014, ApJ, 780, 59
Gratton, R. G., Lucatello, S., Sollima, A., et al. 2013, A&A, 549, A41
Green, G. M., Schlafly, E., Zucker, C., Speagle, J. S., & Finkbeiner, D. 2019, ApJ, 887, 93
Grundahl, F., Stetson, P. B., & Andersen, M. I. 2002, A&A, 395, 481
Hansen, B. M. S., Kalirai, J. S., Anderson, J., et al. 2013, Natur, 500, 51
Haschke, R., Grebel, E. K., & Duffau, S. 2011, AJ, 141, 158
Hawkins, K., Leistedt, B., Bovy, J., & Hogg, D. W. 2017, MNRAS, 471, 722
Hidalgo, S. L., Pietrinferni, A., Cassisi, S., et al. 2018, ApJ, 856, 125
Hoffmann, S. L., Macri, L. M., Riess, A. G., et al. 2016, ApJ, 830, 10
Humphreys, E. M. L., Reid, M. J., Moran, J. M., Greenhill, L. J., & Argon, A. L. 2013, ApJ, 775, 13
Inno, L., Bono, G., Matsunaga, N., et al. 2016, ApJ, 832, 176
Jang, I. S., & Lee, M. G. 2017a, ApJ, 835, 28
Jang, I. S., & Lee, M. G. 2017b, ApJ, 836, 74
Johnson, C. I., McDonald, I., Pilachowski, C. A., et al. 2015, AJ, 149, 71
Jönsson, H., Allende Prieto, C., Holtzman, J. A., et al. 2018, AJ, 156, 126
Joshi, Y. C., & Panchal, A. 2019, A&A, 628, A51
Jurcsik, J. 1995, AcA, 45, 653
Kunder, A., Rich, R. M., Koch, A., et al. 2016, ApJL, 821, L25
Lee, Y.-W., Demarque, P., & Zinn, R. 1994, ApJ, 423, 248
Lindegren, L., Hernández, J., Bombrun, A., et al. 2018, A&A, 616, A2
Macri, L. M., Ngeow, C.-C., Kanbur, S. M., Mahzooni, S., & Smitka, M. T. 2015, AJ, 149, 117
Macri, L. M., Stanek, K. Z., Bersier, D., Greenhill, L. J., & Reid, M. J. 2006, ApJ, 652, 1133
Majewski, S. R., Schiavon, R. P., Frinchaboy, P. M., et al. 2017, AJ, 154, 94
Marino, A. F., Milone, A. P., Casagrande, L., et al. 2016, MNRAS, 459, 610
Marino, A. F., Milone, A. P., Przybilla, N., et al. 2014, MNRAS, 437, 1609
McKeever, J. M., Basu, S., & Corsaro, E. 2019, ApJ, 874, 180
McQuinn, K. B. W., Boyer, M., Skillman, E. D., & Dolphin, A. E. 2019, ApJ, 880, 63
McWilliam, A., & Zoccali, M. 2010, ApJ, 724, 1491
Miglio, A., Brogaard, K., Stello, D., et al. 2012, MNRAS, 419, 2077
Milone, A. P., Marino, A. F., Dotter, A., et al. 2014, ApJ, 785, 21
Milone, A. P., Marino, A. F., Renzini, A., et al. 2018, MNRAS, 481, 5098
Milone, A. P., Piotto, G., Bedin, L. R., et al. 2012, ApJ, 744, 58
Milone, A. P., Piotto, G., Renzini, A., et al. 2017, MNRAS, 464, 3636
Monson, A. J., Beaton, R. L., Scowcroft, V., et al. 2017, AJ, 153, 96
Mould, J., Clementini, G., & Da Costa, G. 2019, PASA, 36, e001
Mucciarelli, A. 2014, AN, 335, 79
Nataf, D. M., Cassisi, S., & Athanassoula, E. 2014, MNRAS, 442, 2075
Nataf, D. M., Gonzalez, O. A., Casagrande, L., et al. 2016, MNRAS, 456, 2692
Nataf, D. M., Gould, A., Pinsonneault, M. H., & Stetson, P. B. 2011, ApJ, 736, 94
Nataf, D. M., Udalski, A., Gould, A., Fouqué, P., & Stanek, K. Z. 2010, ApJL, 721, L28
Nataf, D. M., Wyse, R. F. G., Schiavon, R. P., et al. 2019, AJ, 158, 14
Neeley, J. R., Marengo, M., Freedman, W. L., et al. 2019, MNRAS, 490, 4254
Neugebauer, G., Habing, H. J., van Duinen, R., et al. 1984, ApJL, 278, L1
Nidever, D. L., Bovy, J., Bird, J. C., et al. 2014, ApJ, 796, 38
Nidever, D. L., Hasselquist, S., Hayes, C. R., et al. 2020, ApJ, 895, 88
Nishiyama, S., Nagata, T., Tamura, M., et al. 2008, ApJ, 680, 1174
Nogueras-Lara, F., Schödel, R., Gallego-Calvente, A. T., et al. 2020, NatAs, 4, 377
Paczyński, B., & Stanek, K. Z. 1998, ApJL, 494, L219
Parisi, M. C., Geisler, D., Carraro, G., et al. 2016, AJ, 152, 58
Perryman, M. A. C., Lindegren, L., Kovalevsky, J., et al. 1997, A&A, 500, 501
Piatti, A. E., & Geisler, D. 2013, AJ, 145, 17
Pietrinferni, A., Cassisi, S., & Salaris, M. 2010, A&A, 522, A76
Pietrinferni, A., Cassisi, S., Salaris, M., & Castelli, F. 2004, ApJ, 612, 168
Pietrinferni, A., Cassisi, S., Salaris, M., & Castelli, F. 2006, ApJ, 642, 797
Pietrukowicz, P., Kozłowski, S., Skowron, J., et al. 2015, ApJ, 811, 113
Pietrzyński, G., Graczyk, D., Gallenne, A., et al. 2019, Natur, 567, 200
Queiroz, A. B. A., Anders, F., Chiappini, C., et al. 2020, A&A, 638, A76
Reid, M. J., Pesce, D. W., & Riess, A. G. 2019, ApJL, 886, L27
Reimers, D. 1975, MSRSL, 8, 369
Riess, A. G., Casertano, S., Yuan, W., Macri, L. M., & Scolnic, D. 2019, ApJ, 876, 85
Riess, A. G., Macri, L. M., Hoffmann, S. L., et al. 2016, ApJ, 826, 56
Rubele, S., Pastorelli, G., Girardi, L., et al. 2018, MNRAS, 478, 5017
Salaris, M., Cassisi, S., & Pietrinferni, A. 2016, A&A, 590, A64
Salaris, M., & Girardi, L. 2002, MNRAS, 337, 332

Sarajedini, A., Bedin, L. R., Chaboyer, B., et al. 2007, AJ, 133, 1658
Schlafly, E. F., & Finkbeiner, D. P. 2011, ApJ, 737, 103
Schlegel, D. J., Finkbeiner, D. P., & Davis, M. 1998, ApJ, 500, 525
Schönrich, R., McMillan, P., & Eyer, L. 2019, MNRAS, 487, 3568
Skowron, D. M., Soszyński, I., Udalski, A., et al. 2016, AcA, 66, 269
Skowron, D. M., Skowron, J., Udalski, A., et al. 2021, ApJS, 252, 23
Skrutskie, M. F., Cutri, R. M., Stiening, R., et al. 2006, AJ, 131, 1163
Soszynski, I., Poleski, R., Udalski, A., et al. 2008, AcA, 58, 163
Soszyński, I., Udalski, A., Szymański, M. K., et al. 2016, AcA, 66, 131
Stanek, K. Z., & Garnavich, P. M. 1998, ApJL, 503, L131
Stanek, K. Z., Udalski, A., SzymaŃski, M., et al. 1997, ApJ, 477, 163
Stetson, P. B., Bruntt, H., & Grundahl, F. 2003, PASP, 115, 413
Subramanian, S., & Subramaniam, A. 2012, ApJ, 744, 128
Tang, J., Bressan, A., Rosenfield, P., et al. 2014, MNRAS, 445, 4287
Thompson, I. B., Udalski, A., Dotter, A., et al. 2020, MNRAS, 492, 4254
Thygesen, A. O., Sbordone, L., Andrievsky, S., et al. 2014, A&A, 572, A108
Udalski, A., Soszynski, I., Szymanski, M. K., et al. 2008a, AcA, 58, 89
Udalski, A., Soszyński, I., Szymański, M. K., et al. 2008b, AcA, 58, 329
Ulaczyk, K., Szymański, M. K., Udalski, A., et al. 2013, AcA, 63, 159
Urbaneja, M. A., Kudritzki, R. P., Gieren, W., et al. 2017, AJ, 154, 102
Van der Swaelmen, M., Hill, V., Primas, F., & Cole, A. A. 2013, A&A, 560, A44
Villanova, S., Carraro, G., Geisler, D., Monaco, L., & Assmann, P. 2018, ApJ, 867, 34
Wegg, C., Gerhard, O., & Portail, M. 2015, MNRAS, 450, 4050
Weisz, D. R., Dolphin, A. E., Skillman, E. D., et al. 2013, MNRAS, 431, 364
Wielgórski, P., Pietrzyński, G., Gieren, W., et al. 2017, ApJ, 842, 116
Yanchulova Merica-Jones, P., Sandstrom, K. M., Johnson, L. C., et al. 2017, ApJ, 847, 102
Yuan, W., Riess, A. G., Macri, L. M., Casertano, S., & Scolnic, D. M. 2019, ApJ, 886, 61
Zaritsky, D., Kennicutt Robert, C., Jr., & Huchra, J. P. 1994, ApJ, 420, 87